# NASA TECHNICAL MEMORANDUM 101673
# AVSCOM TECHNICAL MEMORANDUM 89-B-011

# FATIGUE DELAMINATION ONSET PREDICTION IN TAPERED COMPOSITE LAMINATES

Gretchen Bostaph Murri, Satish A. Salpekar, and T. Kevin O'Brien

December 1989

**NASA**

National Aeronautics and
Space Administration

**Langley Research Center**
Hampton, Virginia 23665

**US ARMY
AVIATION
SYSTEMS COMMAND
AVIATION R&T ACTIVITY**

ABSTRACT

Tapered [0°] laminates of S2/CE9000 and S2/SP250 glass/epoxies, and two different specimen types of IM6/1827I, a graphite/epoxy with a toughened interleaf, were tested. Specimens were tested in cyclic tension in a hydraulic load frame. The specimens usually showed some initial stable delaminations in the tapered region, but these did not affect the stiffness of the specimens, and loading was continued until the specimens either delaminated unstably, or reached $10^6$ to $2 \times 10^7$ cycles with no unstable delamination. The final unstable delamination originated at the junction of the thin and tapered regions, and extended into both the tapered and thin regions.

A finite element model was developed for the tapered laminate, both for the undamaged case, and for the tapered laminate with the initial stable delaminations observed in the tests. The analysis showed that for both cases the most likely place for an opening (Mode I) delamination to originate is at the junction of the taper and thin regions. For each material type, the models were used to calculate the strain energy release rate, G, associated with delaminations originating at that junction and growing either into the thin region between the belt and core plies, or into the tapered region, between the belt and dropped plies. The highest values of G were calculated for the laminate with an initial stable delamination in the tapered region and an opening mode delamination growing from the junction into the tapered region.

For the materials tested, cyclic $G_{Imax}$ values from DCB tests were used with the maximum strain energy release rates calculated from the finite element analysis to predict the onset of unstable delamination at the junction as a function of fatigue cycles. The predictions were compared to experimental values of maximum cyclic load as a function of cycles to unstable delamination

from fatigue tests in tapered laminates. For the IM6/1827I and the S2/SP250 laminates, the predictions agreed very well with the test data. Predicted values for the S2/CE9000 were conservative compared to the test data.

## INTRODUCTION

Laminated composite structures with tapered thicknesses are currently being designed as a means of tailoring composite parts for specific performance requirements. The thickness of the laminates is typically reduced by dropping plies internally. However, these ply-drop locations are sources for delamination initiation under bending and tension loads. The low delamination durability of such configurations can result in high costs for repair and replacement of parts. In order to design tapered components with improved resistance to such delamination damage, analyses that model the failure mechanism are necessary.

In this study, the effect of tension fatigue loading on tapered laminates was investigated. Tapered specimens were manufactured from three different material types: S2/SP250 and S2/CE9000 glass/epoxies, and IM6/1827I, a graphite/epoxy which had an interleaf material at the delaminating interface. This interleaf is a toughened thermoset which inhibits delamination growth in laminates under static loads [1]. As fig. 1 shows, under a tension load the continuous belt plies in the tapered region will try to straighten out. The test specimens were loaded in tension fatigue until they either delaminated unstably (as shown in fig. 1), or reached between $10^6$ and $2 \times 10^7$ cycles with no unstable delamination. In order to isolate the effect of the geometric discontinuity at the taper, and avoid the influences of matrix cracks and Poisson's ratio mismatch at the free edge that can occur in many multi-angle laminates, all test specimens were fabricated with unidirectional $[0^o]$ plies only. The fatigue tests produced a curve relating the maximum cyclic load to

3

the log of the number of loading cycles at the onset of sudden, unstable delamination.

In addition, a 2D finite element (FE) analysis was used to calculate interlaminar stresses and strain energy release rates associated with delaminations of the type observed in the experiments. In ref. 2 this finite element analysis was used to model a multi-angle tapered layup under a tension load. The analysis showed that the most likely location for delaminations to initiate was at the junction of the tapered and thin sections (point C in fig. 1). The analysis also showed that a delamination growing from this location initially had a strong Mode I component. This failure mode was also expected in the [0°] tapered laminates because the taper geometry was identical.

In Reference 3, double cantilever beam (DCB) tests were conducted in fatigue to characterize the delamination fatigue behavior of the test materials. These DCB tests produced a curve relating the maximum Mode I cyclic strain energy release rate, $G_{Imax}$, to the corresponding number of loading cycles, N, at which delamination growth begins. In this study, the data from [3] were used with the calculated total strain energy release rates from the finite element analysis to predict the sudden unstable delamination in 0° tapered layups subjected to constant amplitude cyclic loads.

### NOMENCLATURE

| | |
|---|---|
| a | delamination length along taper |
| b | delamination length in thin region |
| $E_{11}$, $E_{22}$ | Young's moduli parallel and transverse to the fiber direction |

| | |
|---|---|
| h | thickness of one ply |
| $G$ | total strain energy release rate |
| $G_I$ | mode I strain energy release rate |
| $G_{II}$ | mode II strain energy release rate |
| $G_{Imax}$ | mode I cyclic strain energy release rate |
| $G_{12}$ | shear modulus |
| $N$ | number of loading cycles to delamination onset |
| $N_x$ | total load per unit width on symmetric half-laminate |
| $P_{max}$ | maximum cyclic load on tapered laminates |
| $R$ | ratio of minimum to maximum applied load |
| $V_f$ | laminate fiber volume fraction |
| $w$ | specimen width |
| $\beta$ | taper angle |
| $\nu_{12}$ | Poisson's ratio |
| $\sigma_o$ | applied tensile stress |
| $\sigma_n$ | interlaminar normal stress |
| $\tau_{nt}$ | interlaminar shear stress |

## EXPERIMENTS

Materials

Panels were made of three different materials: S2/SP250, a 250°F cured glass epoxy; S2/CE9000, a 350°F cured glass epoxy; and IM6/1827I, a 350°F cured graphite epoxy with a toughened thermoset adhesive layer, or interleaf, on one side of the prepreg. The S2/SP250 was manufactured by the 3M company, the S2/CE9000 was manufactured by Ferro Corporation, and the IM6/1827I was manufactured by American Cyanamid. Eight-ply thick, flat panels were laid up in 0°, 90°, and ±45° orientations, cured, cut into coupons, and then were tested to measure lamina moduli and Poisson's ratio. Tapered panels were laid up at NASA Langley, in a tool supplied by Bell Helicopter Textron, such that the center of the panel was thicker than the two ends. All panels were cured according to the manufacturers' recommended curing cycle.

Figure 2 shows a drawing of a laminate cut from a cross section of the tapered panel. The laminates had 38 plies in the center thick region, and 26 plies in the thin region near either end. The transition between the thick and thin regions was accomplished by dropping the internal plies two at a time, forming tapered regions that matched the angle, $\beta$, of the tool. One inch wide strips were cut from each panel, and then cut in the middle of the thick region (fig. 2) to yield two test coupons, each ten inches long.

Figure 3 shows a schematic of the upper half of the tapered laminate, with the thick, tapered, and thin regions indicated. Each region had a length of

sixty-ply thicknesses, 60h. The interior plies that run the entire length of the laminate are referred to as the core region, and the exterior plies, which also run the entire length of the laminate, enclosing the dropped and core plies, are called the belt plies, as indicated in fig. 3. Figure 3 also shows the details in the tapered region. The internal plies were dropped at three locations, forming three regions in the taper, each having a length of 20h, and yielding a taper angle, $\beta$, of 5.71°. Small resin pockets, with triangular cross sections, were assumed to form at the end of each pair of dropped plies. Figure 4 shows photographs of the edge of the tapered region for laminates of the three materials. In all cases, resin pockets are visible at the end of the terminated plies. However, depending on the accuracy of the layup, the two plies of a dropped pair often were not aligned exactly with each other, or the dropped plies were not aligned with the corresponding pair on the other side of the midplane. Furthermore, during the curing process, some of the belt plies and core plies either expanded to accommodate the resin flow, or assumed a curvature to facilitate a smoother transition from the thick to the thin regions. (See fig. 5). Hence, the tapered geometry in fig. 3 was an idealized approximation of the actual detail in the tapered region of the laminates that were manufactured.

For this study, only 0° unidirectional tapered panels were tested so that only the contribution of the taper to the onset of delamination could be studied. However, the IM6/1827I graphite epoxy laminates were made using two different sequences of interleaf orientations. This resulted in two types of laminates, designated C and T (fig.6).

The "C" laminates were laid-up so that the interleaf on all the prepreg plies faced towards the midplane, i.e., towards the center line of the laminate thickness as shown in fig. 6a, where the location of the interleaf layer is indicated by the arrowhead. Hence, in the "C" laminates, the tough interleaf was present at every interface.

The "T" laminates were laid-up such that the interleaf in the belt plies and core plies all faced the laminate midplane, as in the "C" laminates, but the interleaf in the pairs of dropped plies in the tapered region all faced towards each other, as indicated by the arrows in fig. 6b. Hence, in the "T" laminates there was interleaf at the interface between the belt and core plies in the thin region and between the belt and dropped plies in the tapered region, however, there was no interleaf between the core and dropped plies in the tapered region.

## Static Tests

Static tests were conducted on five flat laminates of each material to determine the basic material properties, and on two tapered laminates of each material to determine the elastic moduli of the thin and thick regions. Specimens were loaded in a servo-hydraulic load frame and instrumented with extensometers and strain gages. Strips of emery cloth were wrapped longitudinally around the specimen ends, covering the laminate width on both sides in the grips, to protect the laminate from being damaged by the grip teeth. The hydraulic grip pressure was set at 700 psi for the glass/epoxy laminates and at 1000 psi for the graphite/epoxy laminates.

8

Figure 7a shows the two one-inch long extensometers that were mounted on the thin and thick regions of the tapered laminates to measure the longitudinal modulus of each region. Specimens were loaded in stroke control at a rate of 0.01 inches/minute. The load versus displacement plot for the thin and thick regions was recorded on an X-Y-Y' recorder during the loading.

Fatigue Tests

Tapered specimens were loaded in a servo-hydraulic load frame in the same manner as in the static tests and instrumented with an extensometer mounted over the tapered region to detect delamination onset (fig. 7b). Specimens were loaded statically in load control to the mean load, and then cycled sinusoidally at a maximum constant load amplitude corresponding to an R ratio of 0.1 at a frequency of 5 Hz. Specimens were cycled until the onset of unstable delamination was detected visually, audibly, or by monitoring an increase in displacement in the tapered region. The latter technique was automated by monitoring a change in the voltage output of the extensometer. If a prescribed displacement change was exceeded, the function generator stopped the loading, and the number of loading cycles was recorded. Using this technique, tests could run unattended and the machine would detect the onset of delamination at the junction of the thin and tapered regions. This was always an unstable delamination, and hence, was easily detected. Tests were run for several load levels to determine the number of cycles to unstable delamination onset as a function of the applied maximum cyclic load.

In ref. 2 a simple 2D finite element model was developed to determine strain energy release rates associated with delamination growth in laminates of the geometry shown in fig. 3. Because the laminates considered in this study consisted of only 0-degree plies, a 2D plain strain analysis was assumed to be sufficiently accurate for studying delamination resulting from the geometric discontinuity in the taper. Also, because of the symmetry of the laminates about the X-axis, it was necessary to model only half of the laminate. The model used eight-noded, isoparametric, parabolic elements with the smallest element size equal to one-quarter of the ply thickness, or h/4. A refined mesh was used near the plydrop locations to capture the influence of the ply discontinuities on interlaminar stresses. A schematic of the mesh is shown in fig. 8, where the dimensions in the Z-direction have been exaggerated for clarity. Collapsed eight-noded elements were used at the tips of the resin pockets. The nodes at the end of the thin region were constrained to zero displacement in both the X- and Z- directions and a uniform load per unit width of $N_x$=1000 lb/in. was applied to the half-thickness.

Because the continuous belt plies in the taper region of the laminate are at an angle $\beta$ to the global coordinate system of the laminate, the moduli of these belt plies must be transformed through the taper angle. This transformation is explained in Appendix A.

Strain energy release rates were calculated using both the virtual crack-closure technique (VCCT) and using a global energy method. The VCCT method uses

10

the local forces ahead of, and the relative displacements behind, the
delamination tip to calculate the Mode I and Mode II components of the strain
energy release rate, $G_I$ and $G_{II}$, respectively. The global energy method
calculates the total strain energy release rate, G, only. In this method, the
difference in the work terms associated with two delamination lengths is divided
by twice the difference in the delamination lengths. The result is assumed to
be the total strain energy release rate for a delamination midway between these
two locations.

Two different laminate configurations were modeled in this study. The
first model had 7610 nodes and 2382 elements. It represents an undamaged
laminate in which the delamination was allowed to grow from the junction of the
thin and tapered regions (point C in fig. 3), either into the thin or tapered
regions. The delamination is modeled as growing between the belt and dropped
plies a distance "a" as shown in fig. 3, keeping the thin section completely
laminated; or,from point C into the thin section between the belt and core
plies, a distance "b" (fig. 3), allowing no delamination in the tapered region.
Duplicate nodes were created in the model along these interfaces and were
constrained to act together. Different delamination lengths were then modeled
by releasing the appropriate constraints.

A second, modified model, with 7699 nodes and 2382 elements, was developed
to analyze delaminations observed in the test specimens. In this model,
duplicate nodes were created along the interface between the dropped plies and
core section, to the left of point F' in fig. 3, through the taper region, and
along the front edge of the dropped plies, between points F and F'. Those
nodes, as well as those in the taper section between points F and B were
released, creating the configuration shown in fig. 9. As in the first model,

11

different delaminations growing on either side of point C were modeled by releasing the appropriate constraints.

Both models were used to predict strain energy release rates for delamination growth starting at point C in fig. 3, for the S2/SP250, S2/CE9000, and IM6/1827I tapered laminates.

RESULTS AND DISCUSSION

Experiments

Table 1 lists the basic material properties determined from the flat laminate tests. Table 2 lists the average measured longitudinal moduli of the thin and thick regions of the tapered laminates made from each of the three materials. Also listed in Table 2 are the average measured ply thicknesses and volume fractions for the thin and thick regions. The thick regions had larger ply thicknesses, and correspondingly lower fiber volume fractions, than the thin regions. Consequently, the moduli measured in the thin region were higher than the moduli measured in the thick region, and the average of the two measurements was similar to the moduli measured on the flat laminates (Table 1). The lamina properties used in the FE analysis were taken from Table 1. The properties given for the IM6/1827I material in Table 1 represent smeared properties for the fiber reinforced epoxy plus the interleaf. The epoxy plies and interleaf were not discreetly modeled in the analysis. The neat resin properties for a typical epoxy from [4] are also given in Table 1.

12

For all of the IM6/1827I and S2/CE9000 specimens, some initial stable delamination occurred in the specimens before the final, unstable delamination initiated at point C (fig. 3). This preliminary delamination was not observed in the S2/SP250 laminates. As shown in fig.9, the initial delamination began with a resin crack at the tip of the innermost dropped plies, between the end of the plies and the resin pocket. Under continued loading, delaminations then grew stably from this crack through the tapered region toward the thick region, between the core and dropped plies, and between the belt and dropped plies, extending along the length of the taper section and sometimes into the thick section a short distance. These delaminations usually formed on both sides of the mid-plane at a very low number of loading cycles and caused a slight decrease in the stiffness of the test specimens. However, the stiffness loss was not significant in any of the tests, and loading was continued until the final unstable delamination occurred. Reference to figs. 6(a) and 6(b) shows that after this initial delamination occurred, configurations C and T of the IM6/1827I graphite/epoxy were essentially the same. Between points F and D in fig. 3, both types C and T had interleaf along the belt-dropped-ply interface, and between the belt and core plies in the thin region, but not along the core-dropped-ply interface.

The final unstable delamination failure usually occurred along the interface between the belt and dropped plies in the tapered region, (with damage sometimes between the core and dropped plies also), and between the belt and core plies in the thin region. Figure 10 shows a photo of the damage in the vicinity of point C for a type T graphite specimen. Unstable delamination was usually evident on both sides of the laminate mid-plane; however, it was usually more extensive on one side, with the delaminations extending further and occasionally with delaminations at other interfaces. For specimens where the

13

innermost dropped plies were not terminated at locations symmetric about the midplane, the most extensive damage occurred on the side where the dropped plies extend further toward the thin region.

Figures 11-14 show the maximum cyclic loads vs. number of loading cycles to unstable delamination onset for each of the four different specimen types tested. Types T and C of the graphite/epoxy specimens showed similar results with moderate scatter (fig. 11,12). Arrows on the data points indicate that the test was terminated before the specimen delaminated. Figures 13 and 14 show the results for the S2/CE9000 and S2/SP250 tests, respectively. The results show little scatter, with the S2/SP250 specimens having slightly longer lives than the S2/CE9000 for the same maximum cyclic load.

## Finite Element Model

The finite element model was used to calculate interlaminar normal and shear stress distributions using the three sets of material properties and the epoxy neat resin properties given in Table 1. Results for the undamaged laminate are shown in figs. 15 and 16 for the IM6/1827I material. Figure 15 shows the interlaminar normal stress along interface ABCD normalized by the applied tensile stress $(\sigma_n/\sigma_o)$. The results suggest that stress singularities may exist at the ply drop locations, as demonstrated by the steep peaks at those locations. However, for the same mesh refinement, the magnitude was highest at point C, with the interlaminar normal stresses tensile on both sides, indicating that point C is the most likely place for a Mode I delamination to start. Figure 16 shows the normalized interlaminar shear stresses $(\tau_{nt}/\sigma_o)$ along the

same interface. The shear stresses show high peaks at the ply drop locations. These results are consistent with the results of [2] for a glass/epoxy laminate that was not unidirectional. Therefore it is apparent that these results are due to the taper configuration and not the layup or material modeled.

Interlaminar normal and shear stresses were also calculated for a second model with a resin crack between points F and F' (see fig. 3) between the end of the dropped plies and the adjacent resin pocket, as shown by the inset in figs. 17 and 18. Figure 17 suggests that singularities may exist at the ply drops. As in fig. 15, stresses on both sides of point C are tensile. Therefore, the initial delamination damage does not seem to change the location where the final unstable delamination begins. Comparison of figs. 16 and 18 shows that for the resin crack configuration, the interlaminar shear stresses again show peaks at the ply drop locations, but the shear stress to the right of point F becomes compressive very close to the resin crack. The distribution of interlaminar normal and shear stresses for the two glass materials was similar to the graphite.

For each of the three material systems, the finite element model was used to calculate G as a delamination was extended into the taper or thin regions. Delaminations that extended into the taper, along the belt and dropped ply interface from point C, were designated of length a as shown in fig. 3. Delaminations into the thin section, along the belt and core interface from point C, were designated of length b as shown in fig. 3. First, a delamination was assumed to grow in the tapered section, from point C between the belt and dropped plies, with no delamination in the thin section (b=0). At each new delamination length a, G was calculated. Similarly, delamination growth into the thin section with no delamination in the tapered section (a=0) was modeled, and values of G were calculated. Calculations were performed for

15

both the undamaged laminate model and for the laminate model with initial delaminations. In all cases the results are given as a normalized value of $Gh/N_x^2$ in order to permit easier comparison between configurations with different thicknesses or applied loads. Results are shown for the undamaged model with the IM6/1827I material in fig. 19. Results given for both the VCCT and energy based methods show good agreement. Similar good agreement between the VCCT and energy based results was found for all the cases analyzed; therefore in the remainder of the figures, curves are shown which represent the VCCT results only.

As fig. 19 shows, G increases rapidly as the delamination grows in either direction, and reaches a peak after the delamination has grown a few ply thicknesses. As the delamination is allowed to grow further, G drops off. The peak value of G was always higher for delamination growth into the taper section than for growth into the thin section. Figure 20 shows the corresponding results for the initially delaminated laminate along with the results for the undamaged laminate model from fig. 19. As fig. 20 shows, G is higher in the laminate with initial delaminations at every delamination length, with the highest value of G corresponding to delamination growth in the tapered region. This same pattern was observed for all three material systems modeled. Results for the undamaged and initially delaminated models for the S2/CE9000 and S2/SP250 materials are shown in figs. 21 and 22, respectively. As these two figures show, for the initially delaminated models with delamination growing into the taper, G tends to quickly reach a peak, drops slightly, and then continues to rise as the delamination length increases.

Figure 23 shows the ratio of $G_I$ to total G for the tapered laminate modeled, with delamination growth in the tapered region and in the thin region.

16

The initial delamination growth is primarily Mode I for all three materials. The Mode III component for this unidirectional laminate is assumed to be zero. Hence, in fig. 23, as the delamination extends into the taper and the Mode I contribution decreases, the Mode II contribution increases until the Mode II component comprises about 85% of total G near a=20h. For the two glass materials, the percentage of Mode I starts out slightly lower and drops faster, compared to the graphite material, which remains largely Mode I for several ply thicknesses. For all three materials, fig. 23 shows that the delamination growth into the thin region is almost entirely Mode I for all delamination lengths.

## Failure Predictions

In ref. 3, the delamination fatigue behavior of the current test materials under Mode I loading was characterized using DCB tests. The tests were terminated when the initial delamination growth was detected. By testing at various load levels, a curve was generated which related the maximum cyclic strain energy release rate, $G_{Imax}$, to the number of loading cycles, N, at the onset of delamination. These tests were conducted for the three materials used in the current study. Resulting G-N curves are shown in figs. 24-26, and the data are included in Tables 3-5.

An attempt was made to use these G-N data along with the finite element analysis to unstable delamination onset during fatigue for the tapered laminates. It is sufficient to use the measured Mode I data from the DCB tests, since the finite element model showed that the initial delamination growth is almost completely Mode I. Since no attempt was made in [3] to produce a

17

statistical curve fit through the DCB data, and since it was not a goal of this study to produce such a curve, the individual DCB data points were used in these predictions. For each of the three materials, the appropriate finite element model was chosen to match the actual failure behavior observed in the tests. The first peak value of $Gh/N_x^2$ for a delamination growing into the taper region was designated $(Gh/N_x^2)_{FE}$ (Tables 3-5). It was postulated that unstable delamination growth would initiate in the tapered laminate when the total $G$ value calculated from the FE analysis equaled the cyclic $G_{Imax}$ at which delamination initiated in the DCB tests. For each data point shown in figs. 24-26 (and tabulated in Tables 3-5), we can write

$$\left(\frac{Gh}{N_x^2}\right)_{FE} \frac{N_x^2(N)}{h} = G_{Imax}(N) \tag{1}$$

where h is the average measured ply thickness from Table 2 and $N_x(N)$ is the applied maximum cyclic load per unit width on the tapered laminate half-thickness. The maximum cyclic load $P_{max}(N)$ for the tapered laminates is then

$$P_{max}(N) = 2 w N_x(N) \tag{2}$$

where w is the laminate width . Substituting eq. (2) in eq. (1) and solving for $P_{max}(N)$ gives

$$P_{max}(N) = \sqrt{\frac{G_{Imax}(N) h (2w)^2}{\left(\frac{G h}{N_x^2}\right)_{FE}}} \tag{3}$$

18

For each value of N in Tables 3-5, the corresponding $G_{Imax}$ was used in eq. (3) to solve for the predicted maximum cyclic load, $P_{max}$. Tables 3-5 list the values of $(Gh/N_x^2)_{FE}$ and the predicted values of $P_{max}$(N) for each set of DCB data. The predicted maximum cyclic loads and corresponding number of cycles to delamination onset are plotted with the tapered laminate test results in figs. 27-30.

Figures 27 and 28 show the predicted failure loads for types T and C of the IM6/1827I material, along with the actual test data. The predictions are based on the finite element results for the damaged laminate model. The predictions show very good agreement with the test data for both types T and C laminates.

Figure 29 shows the values predicted for the S2/CE9000 laminates using the initially delaminated model, along with the measured failure loads. These predictions are conservative compared to the data. Close examination of the resin pockets of these specimens shows that the plies on both sides of the resin tend to curve in toward the resin, creating a much smaller local taper angle than was modeled. (See fig. 5.) A smaller taper angle in the model would result in lower values of $Gh/N_x^2$; the predicted $P_{max}$(N) values would therefore be higher and would agree more closely with the test data.

For the S2/SP250 laminates the predictions were calculated using results of the undamaged laminate model, since initial stable delamination growth was not observed in the tapered laminate fatigue tests. Figure 30 shows the predictions and test results. The predictions are very good for this case. However, as indicated in fig. 26, the DCB data for this material were generated using R=0.5, rather than R=0.1, as for the other DCB tests and for the tapered laminates. Testing at R=0.1 may have the effect of decreasing the cycles to delamination

19

onset, for the same values of $G_{Imax}$, compared to testing at R-0.5, thereby shifting the data in fig. 26 down slightly. In that case, $P_{max}(N)$ values calculated using R-0.1 data would be slightly lower than the calculated values (from the R-0.5 data,) and the predictions would then actually be more conservative compared to the test data.

The predictions for all the laminates seem reasonable, however, considering that the geometry of the resin pocket is very idealized. As discussed in the materials section, the resin pocket geometry of the laminates may be quite different from the model due to problems associated with the lay-up and manufacture of the panels.

The fact that the calculated $Gh/N_x^2$ values decrease after reaching a peak, seems to indicate that stable delamination growth should be expected in the tapered laminates. However, it was shown in [2] that the calculated peak value of G for delamination growth into the taper (or thin) region increases as the fixed delamination length in the thin (or taper) region increases. Therefore the strain energy release rate increases continually as the delamination grows in either direction from point C. This results in unstable delamination growth initiating at point C and growing in both directions.

CONCLUSIONS


Tapered [0°] laminates of four different types were tested in cyclic

tension until they delaminated. The specimens types consisted of S2/CE9000

glass/epoxy, S2/SP250 glass/epoxy, and two different specimen types of IM6/1827I

graphite/epoxy which had a toughened interleaf material at the delaminating

interfaces. The delaminations originated at the junction of the tapered and

thin sections and grew unstably, both along the taper and into the thin region.

A finite element model of the tapered laminate was used to calculate strain

energy release rates associated with delamination growth along these interfaces

for each of the materials tested. The model showed that the initial

delamination is primarily Mode I for all the cases. In addition, DCB test data

were used to characterize the Mode I fatigue delamination behavior of the

materials. The DCB results were used along with the finite element calculations

to predict delamination onset in the tapered laminates as a function of loading

cycles. The following conclusions were reached:



1. Under tensile fatigue loading, the IM6/1827I and S2/CE9000 tapered laminates

   experienced some initial stable delamination that did not result in

   significant stiffness loss. For all the test laminates the final

   delamination was unstable, initiating at the junction of the thin and

   tapered regions, and growing in both directions at the interface between the

   belt and the underlying plies.

2. Finite element calculations showed that the presence of the initial delamination damage increases the strain energy release rate for unstable delamination from the junction point between the thin and tapered regions.

3. The finite element model, when used with fatigue delamination durability data generated from double cantilever beam fatigue tests did a reasonable job of predicting unstable delamination onset in fatigue for the tapered laminates.

4. For the glass/epoxy tapered laminates delamination onset predictions tended to be conservative. This was probably due to differences between the idealized taper angles that were modeled and the less severe tapered angles that formed in the specimens during manufacture as a result of the expansion and movement of the plies to accommodate the resin flow at the taper.

# REFERENCES

1. Chan, W.S., Rogers, C., and Aker, S., "Improvement of Edge Delamination Strength of Composite Laminates Using Adhesive Layers," in _Composite Materials: Testing and Design_, ASTM STP 893, 1986, p.266.

2. Salpekar, S.A., Raju, I.S., and O'Brien, T.K., "Strain Energy Release Rate Analysis of Delamination in Tapered Laminate Subjected to Tension Load," Proceedings of the American Society for Composites, Third Technical Conference, Seattle, Washington, September 1988, pp.642-654.

3. Martin, R.H. and O'Brien, T.K., "Characterizing Mode I Fatigue Delamination of Composite Materials," Fourth Technical Conference of the American Society for Composites, Blacksburg, Virginia, October 1989, pp.257-266.

4. Shivakumar, K.N. and Crews, J. H., Jr., "Bolt Clampup Relaxation in a Graphite/Epoxy Laminate," in _Long Term Behavior of Composites_, ASTM STP 813, 1983, pp. 5-22.

Appendix A

Transformation of Stiffness Coefficients

The following transformation was used in [2] where tapered laminates with a multi-angle layup were studied. Since the laminates in the current study were all unidirectional, there is no rotation $\theta$ about the 3-axis. However, the complete transformation is included here for a general case.

The stress-strain relations for each lamina are transformed from the material coordinate system 1,2,3 (Fig. 31) to the global system XYZ using the following procedure. The 3D stress-strain relation for a ply in the material coordinate system is

$$\{\sigma\}_{123} = [C] \{\epsilon\}_{123} \qquad (A1)$$

where $\{\sigma\}_{123} = \{\sigma_{11} \quad \sigma_{22} \quad \sigma_{33} \quad \sigma_{12} \quad \sigma_{23} \quad \sigma_{13}\}$;

$$\{\epsilon\}_{123} = \{\epsilon_{11} \quad \epsilon_{22} \quad \epsilon_{33} \quad \epsilon_{12} \quad \epsilon_{23} \quad \epsilon_{13}\};$$

and $[C]_{6x6}$ is a matrix that can be determined from elastic constants. Following similar notations, the stress-strain relations for a lamina in the global system can be written as

$$\{\sigma\}_{XYZ} = [C]' \{\epsilon\}_{XYZ} \qquad (A2)$$

The matrix $[C]'$ is obtained from matrix $[C]$ by rotating the material system 1,2,3 (Fig. 31) to the global coordinate system XYZ through two rotations; a

rotation ($\theta$) about the Z (or 3) axis, and then by a rotation ($\phi$) about the Y (or Y') axis. The transformed stiffness coefficient matrix, [C]', is obtained from the material stiffness coefficient matrix, [C] as

$$[C]'_{6x6} = [T_\phi]_{6x6} \, [T_\theta]_{6x6} \, [C]_{6x6} \, [T_\theta]^T_{6x6} \, [T_\phi]^T_{6x6} \qquad (A3)$$

where $[T_\theta]$ and $[T_\phi]$ are defined in terms of the appropriate angle as

$$[T_\theta] = \begin{vmatrix} \cos^2\theta & \sin^2\theta & 0 & 2*\cos\theta*\sin\theta & 0 & 0 \\ \sin^2\theta & \cos^2\theta & 0 & -2*\cos\theta*\sin\theta & 0 & 0 \\ 0 & 0 & 1.0 & 0 & 0 & 0 \\ -\cos\theta*\sin\theta & \cos\theta*\sin\theta & 0 & \cos^2\theta - \sin^2\theta & 0 & 0 \\ 0 & 0 & 0 & 0 & \cos\theta & -\sin\theta \\ 0 & 0 & 0 & 0 & \sin\theta & \cos\theta \end{vmatrix}$$

and

$$
[T_\phi] = \begin{vmatrix}
\cos^2\phi & 0 & \sin^2\phi & 0 & 0 & 2*\cos\phi*\sin\phi \\
0 & 1.0 & 0 & 0 & 0 & 0 \\
\sin^2\phi & 0 & \cos^2\phi & 0 & 0 & -2*\cos\phi*\sin\phi \\
0 & 0 & 0 & \cos\phi & \sin\phi & 0 \\
0 & 0 & 0 & -\sin\phi & \cos\phi & 0 \\
-\cos\phi*\sin\phi & 0 & \cos\phi*\sin\phi & 0 & 0 & \cos^2\phi - \sin^2\phi
\end{vmatrix}
$$

The superscript T in equation (A3) denotes the transpose of the matrix. Furthermore, the plane strain conditions require that $\epsilon_{YY} = \epsilon_{XY} = \epsilon_{YZ} = 0$. Incorporating these conditions in (A2) yields the stress-strain relations for plane strain as

$$\{\sigma\}_{XZ} = [C]'_{XZ} \{\epsilon\}_{XZ} \qquad (A4)$$

where $\{\sigma\}_{XZ} = \{\sigma_{XX} \quad \sigma_{ZZ} \quad \sigma_{XZ}\}$; $\{\epsilon\}_{XZ} = \{\epsilon_{XX} \quad \epsilon_{ZZ} \quad \epsilon_{XZ}\}$.

and $[C]'_{XZ}$ is obtained from the global $[C]'$ matrix as,

$$
[C]'_{XZ} = \begin{vmatrix}
C'_{11} & C'_{13} & C'_{16} \\
C'_{31} & C'_{33} & C'_{36} \\
C'_{61} & C'_{63} & C'_{66}
\end{vmatrix} \qquad (A5)
$$

26

## Table 1. Material Properties

| | S2/SP250 | S2/CE9000 | IM6/1827I | Neat Resin[4] |
|---|---|---|---|---|
| $E_{11} \times 10^6$ psi | 6.600 | 7.116 | 19.000 | 0.595 |
| $E_{22} \times 10^6$ psi | 2.100 | 2.464 | 0.856 | 0.595 |
| $G_{12} \times 10^6$ psi | 0.880 | 1.100 | 0.615 | 0.224 |
| $\nu_{12}$ | 0.275 | 0.303 | 0.361 | 0.330 |
| $V_f$, % | 57.0 | 59.0 | 53.5 | .... |

## Table 2. Longitudinal moduli of thin and thick regions in tapered laminates

| | $E_{11} \times 10^6$ psi | $\nu_{12}$ | h, in. | $V_f$, % |
|---|---|---|---|---|
| **S2/SP250** | | | | |
| Thin | 7.730 | 0.272 | 0.0079 | 57.3 |
| Thick | 5.990 | 0.229 | 0.0081 | 55.5 |
| **S2/CE9000** | | | | |
| Thin | 7.333 | 0.271 | 0.0074 | 61.2 |
| Thick | 6.782 | 0.223 | 0.0078 | 57.6 |
| **IM6/1827I** | | | | |
| Thin | 20.85 | -- | 0.0079 | 54.7 |
| Thick | 17.39 | -- | 0.0082 | 52.7 |

Table 3.  IM6/1827I graphite/epoxy.

$$\left(Gh/N_x^2\right)_{FE} = 59.0 \times 10^{-12} \; \frac{\text{in-lb}}{\text{in}^2}$$

| G-N data (DCB tests) | | tapered laminate predictions |
|---|---|---|
| $\underline{G}_{Imax}$, in-lb/in$^2$ | N, cycles | P, lbs |
| 1.417 | 7440 | 27,723 |
| 0.800 | 41,150 | 20,830 |
| 0.509 | 1,015,480 | 16,615 |
| 0.417 | 36,840 | 27,723 |
| 0.794 | 78,730 | 20,752 |
| 0.356 | 1,000,000* | 13,895 |
| 0.502 | 1,129,340* | 16,501 |
| 0.510 | 415,650 | 16,632 |
| 0.754 | 30,260 | 20,222 |
| 1.420 | 21,000 | 27,752 |
| 1.370 | 38,410 | 27,259 |
| 0.777 | 65,570 | 20,529 |

Table 4.  S2/CE9000 glass/epoxy.

$$\left(Gh/N_x^2\right)_{FE} = 39.0 \times 10^{-12} \; \frac{\text{in-lb}}{\text{in}^2}$$

| G-N data (DCB tests) | | tapered laminate predictions |
|---|---|---|
| $\underline{G}_{Imax}$, in-lb/in$^2$ | N, cycles | P, lbs |
| 0.096 | 55,000 | 8,651 |
| 0.107 | 212,300 | 9,133 |
| 0.195 | 12,370 | 12,329 |
| 0.070 | 120,024 | 7,387 |
| 0.107 | 44,510 | 9,133 |
| 0.196 | 85,240 | 12,360 |
| 0.100 | 284,570* | 8,829 |
| 0.180 | 25,000 | 11,855 |
| 0.192 | 2,000 | 12,234 |
| 0.286 | 4,000 | 14,931 |

* specimen did not reach unstable failure

Table 5.  S2/SP250 glass/epoxy.

$$(Gh/N_x^2)_{FE} = 37.0 \times 10^{-12} \ \frac{in\text{-}lb}{in^2}$$

| G-N data (DCB tests) | | tapered laminate predictions |
| --- | --- | --- |
| $G_{Imax}$, in-lb/in$^2$ | N, cycles | P, lbs |
| 0.310 | 182,000 | 16,788 |
| 0.223 | 1,486,000* | 14,231 |
| 0.449 | 2,000 | 20,193 |
| 0.347 | 50,000 | 17,751 |
| 0.246 | 1,440,000* | 14,946 |
| 0.260 | 100,000 | 15,366 |
| 0.242 | 148,000 | 14,824 |
| 0.277 | 144,000 | 15,860 |
| 0.167 | 3,449,000* | 12,315 |
| 0.462 | 15,000 | 20,483 |
| 0.392 | 47,000 | 18,867 |
| 0.187 | 8,500,000 | 13,031 |

* specimen did not reach unstable failure
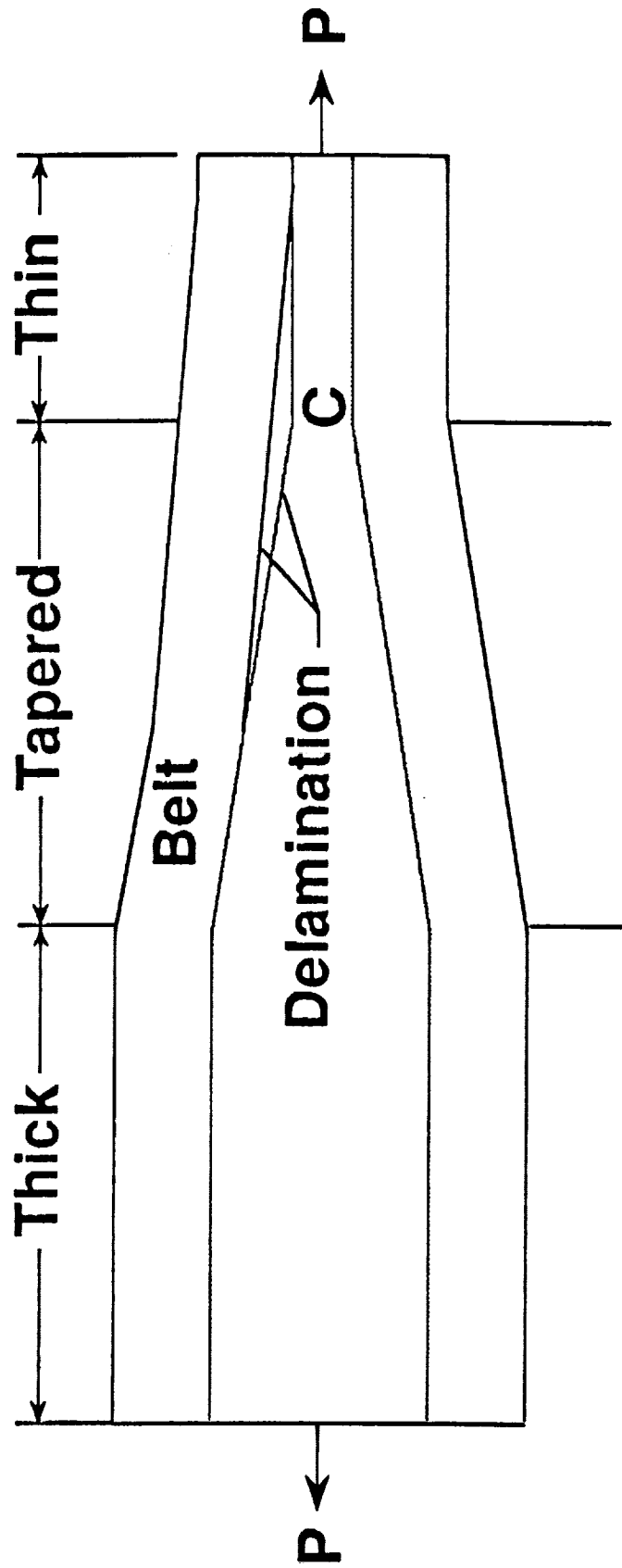
Figure 1. - Delamination growth in tapered laminate with
tension load.

Thin region

Tapered region

Thick region

Cut

Thin region

z,3
y,2
x,1

β

5 in.
1/2 in.
9 in.
1/2 in.
5 in.
20 in.

1 in.
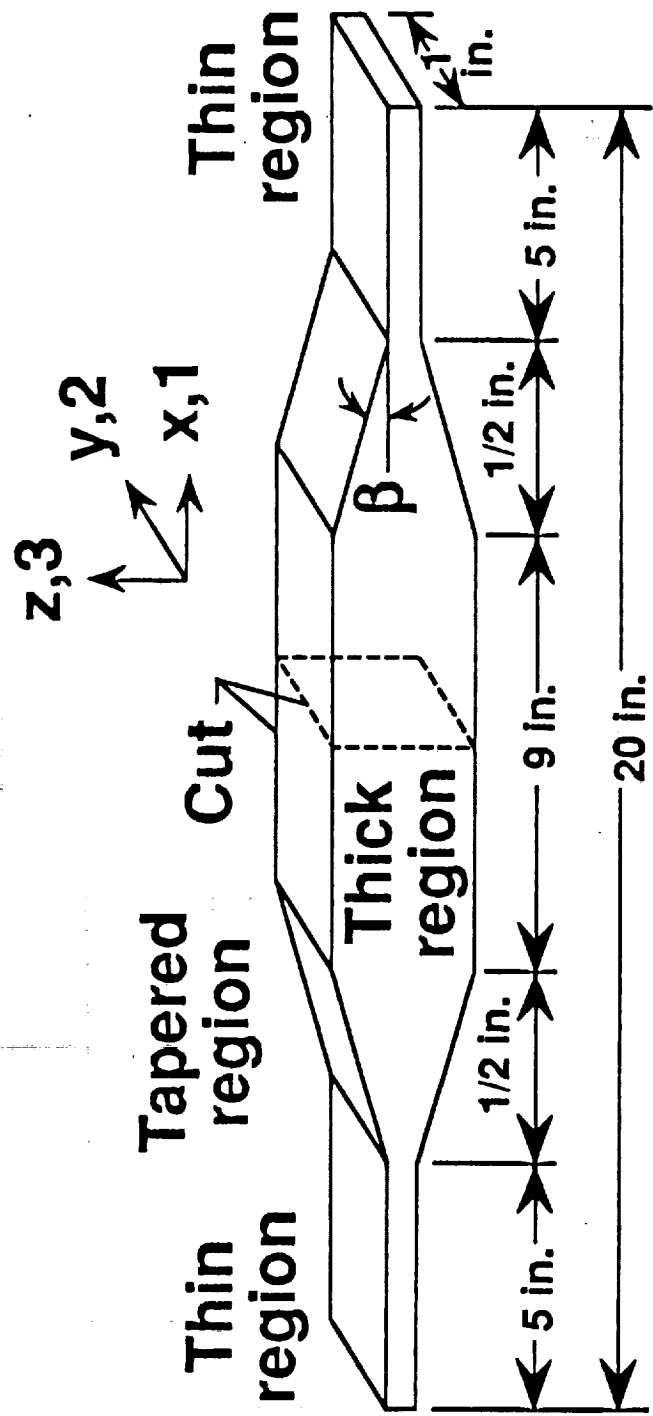
Note: drawing not to scale

Figure 2. - Laminate cut from tapered panel.

31
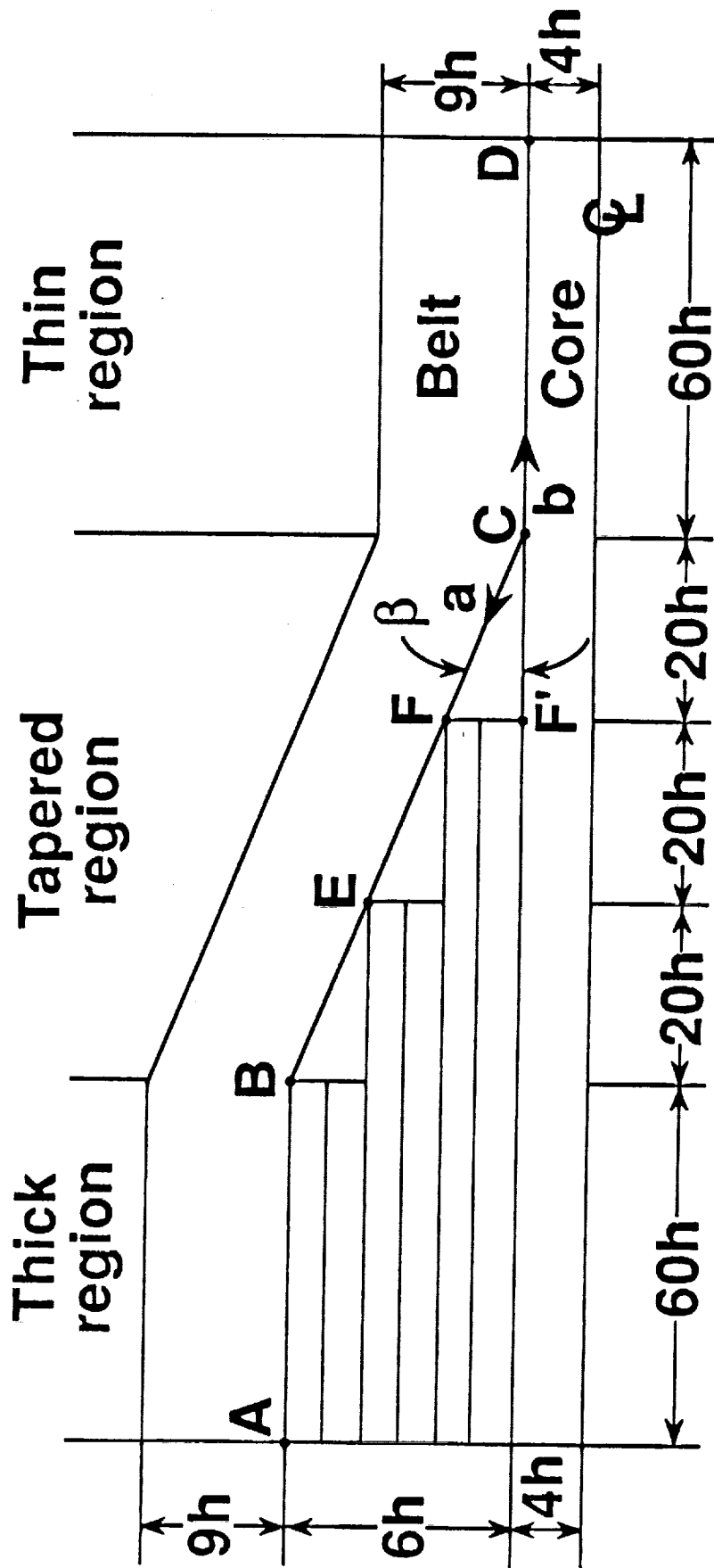
Figure 3. – Tapered laminate with internal ply drops.
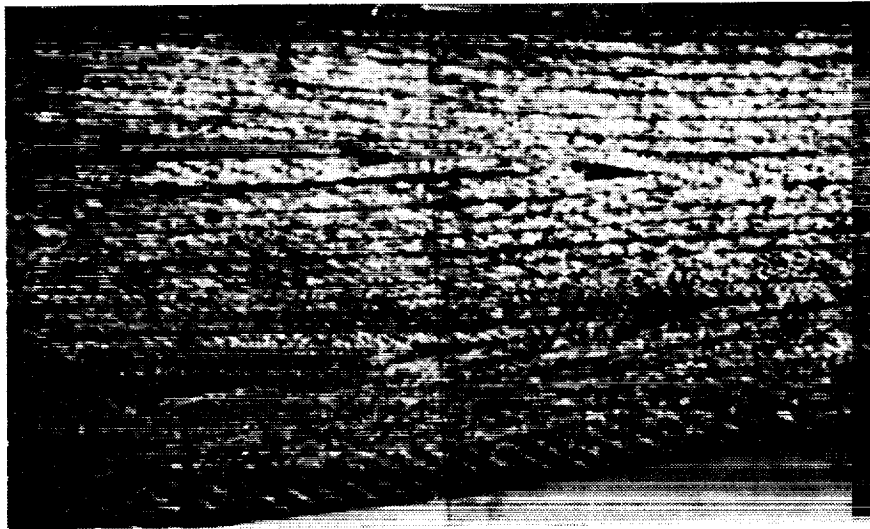
**(a) IM6/1827I**
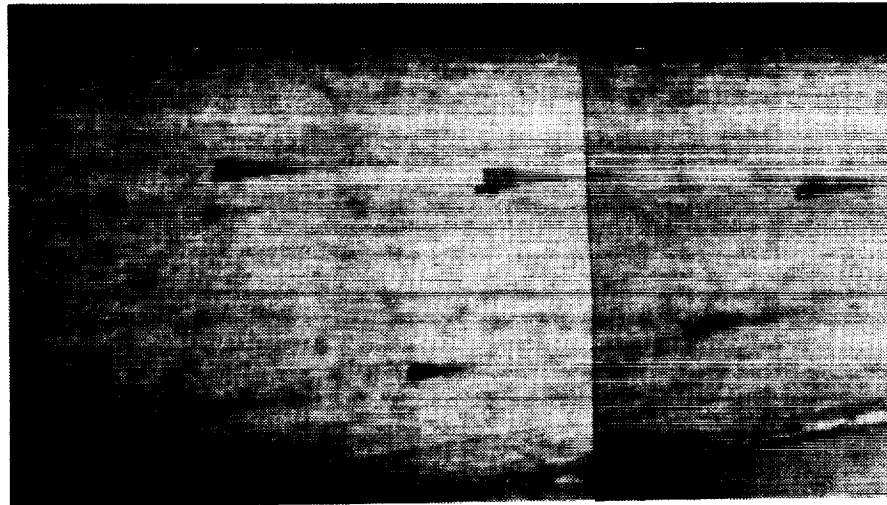


**(b) S2/CE9000**
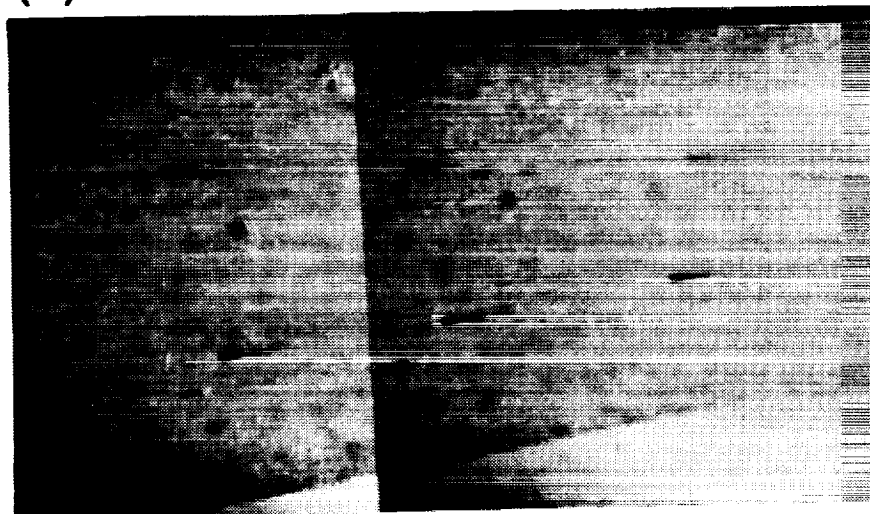


**(C) S2/SP250**

Figure 4. - Photographs of dropped ply locations for three test materials.

33
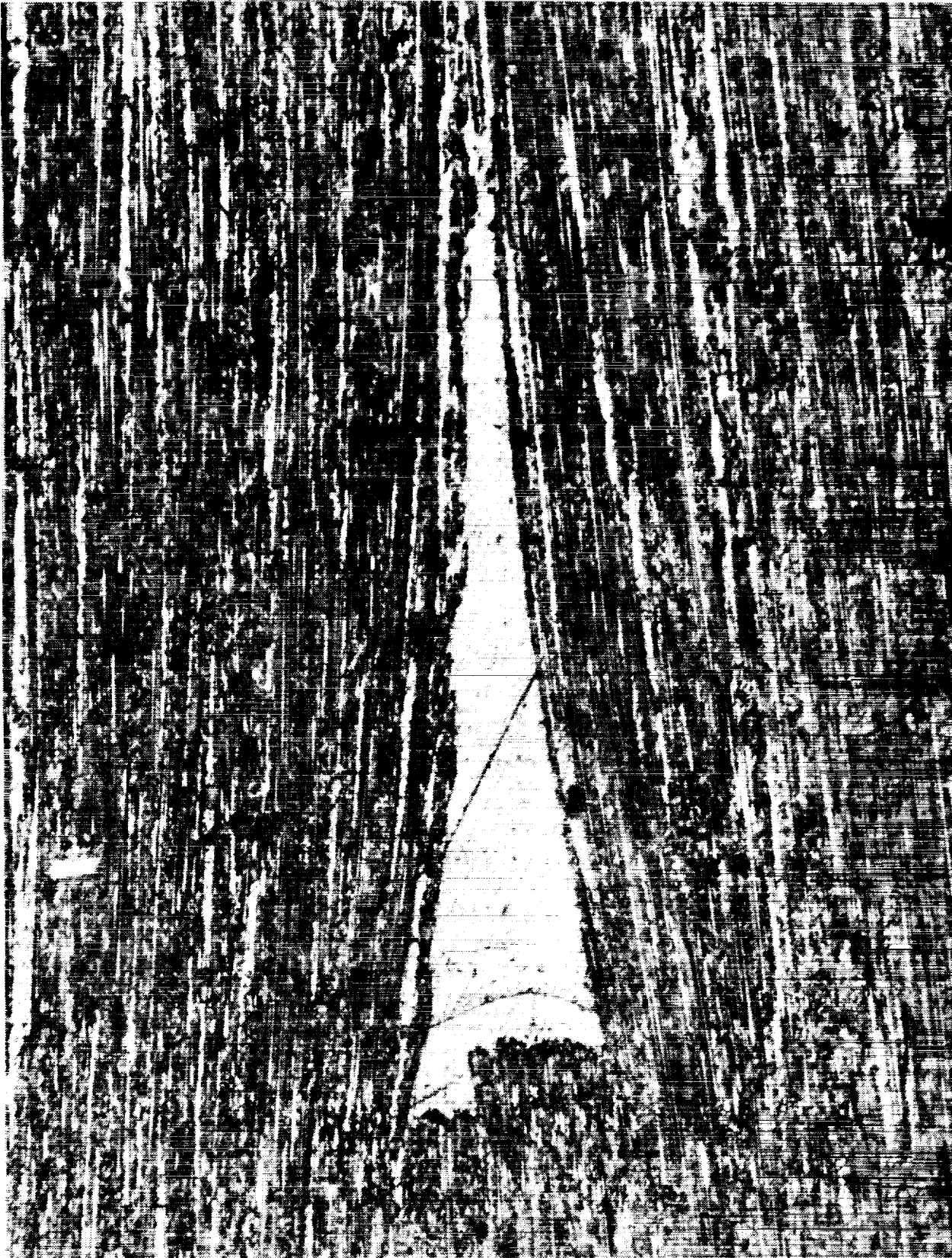
Figure 5. - Resin pocket with curved plies in S2/CE9000.
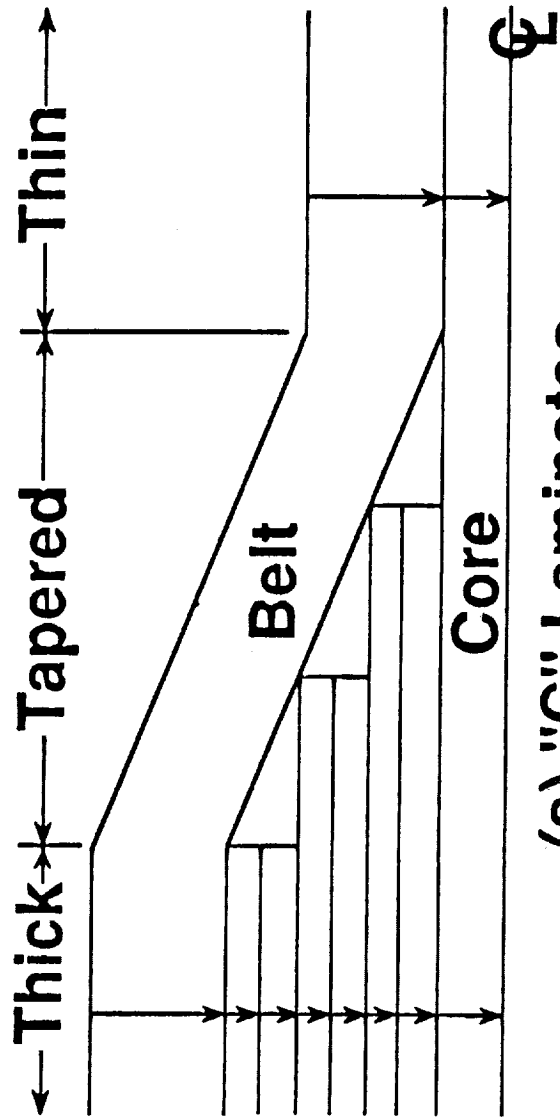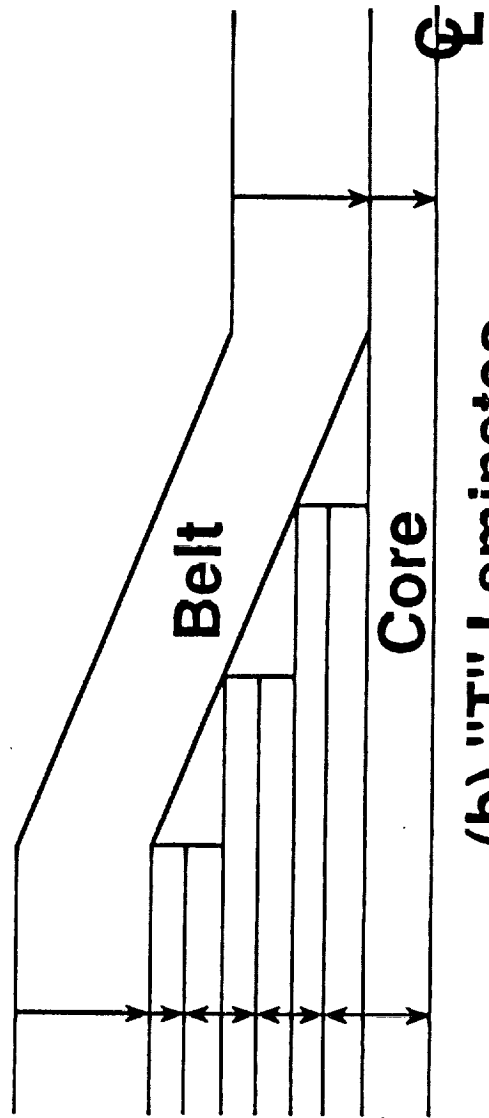
Figure 6. - Interleaf locations in IM6/1827I laminates. Arrows indicate direction of interleaf in plies.

35
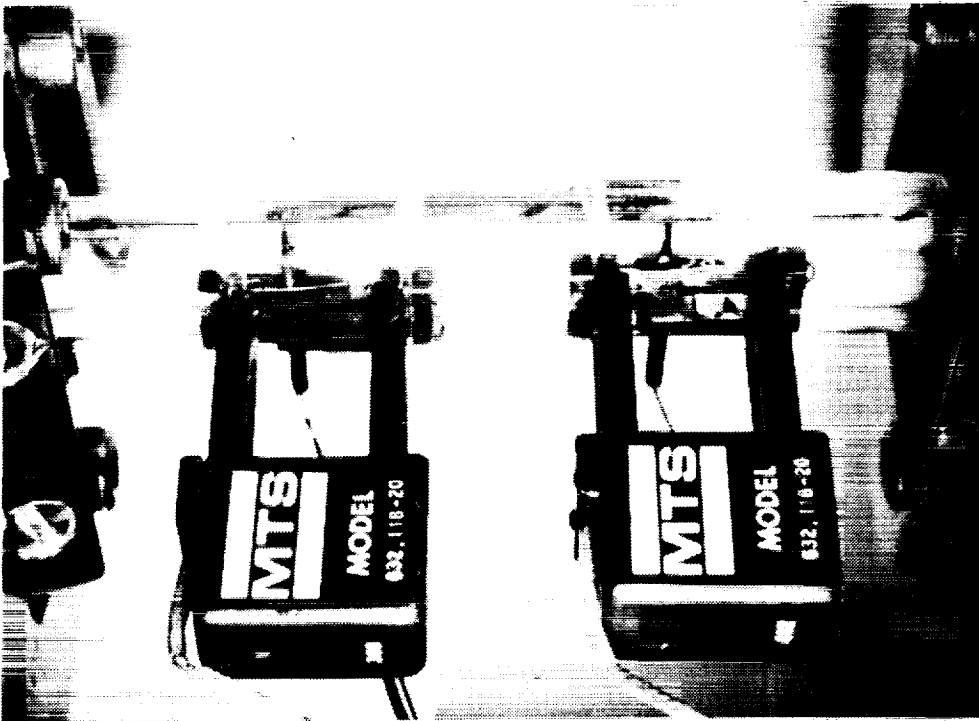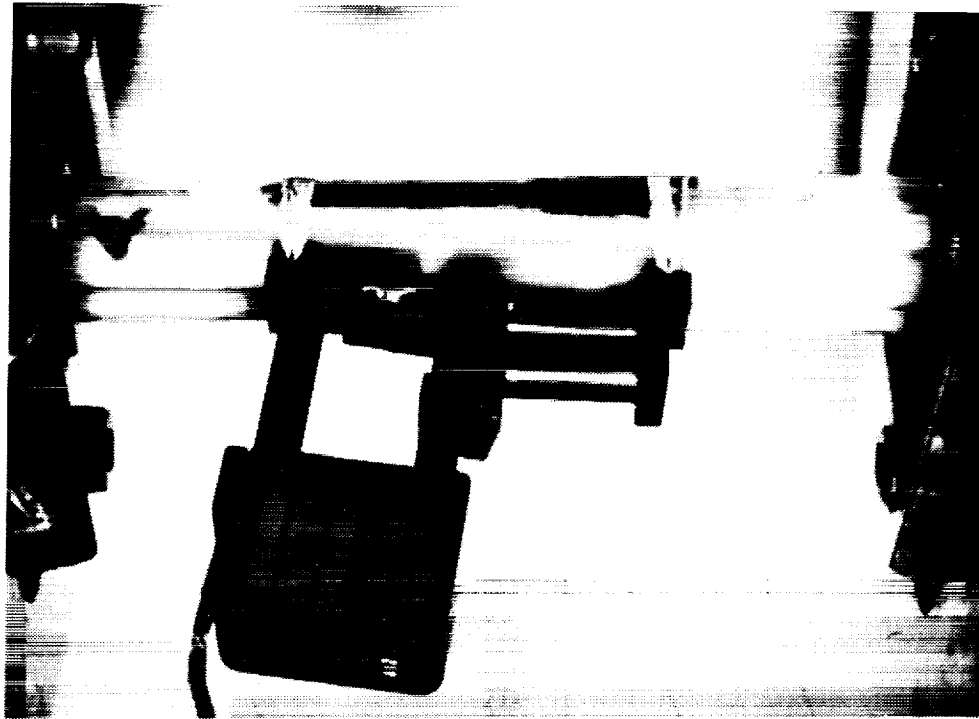
(b) Fatigue test

(a) Static test

Figure 7. - Photographs of test specimens in hydraulic load frame with mounted extensometers.
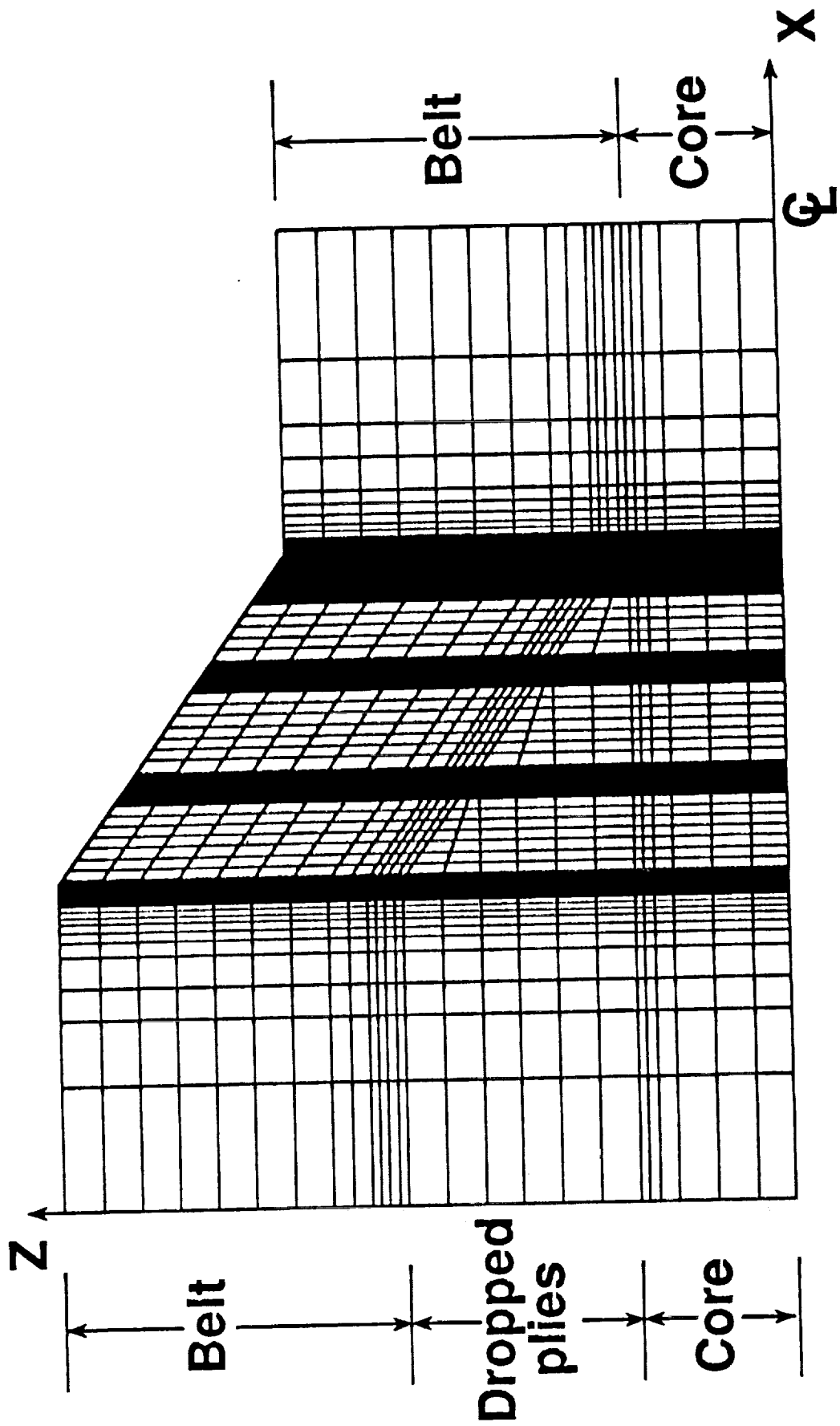
Figure 8. - Finite element model of the tapered laminate.
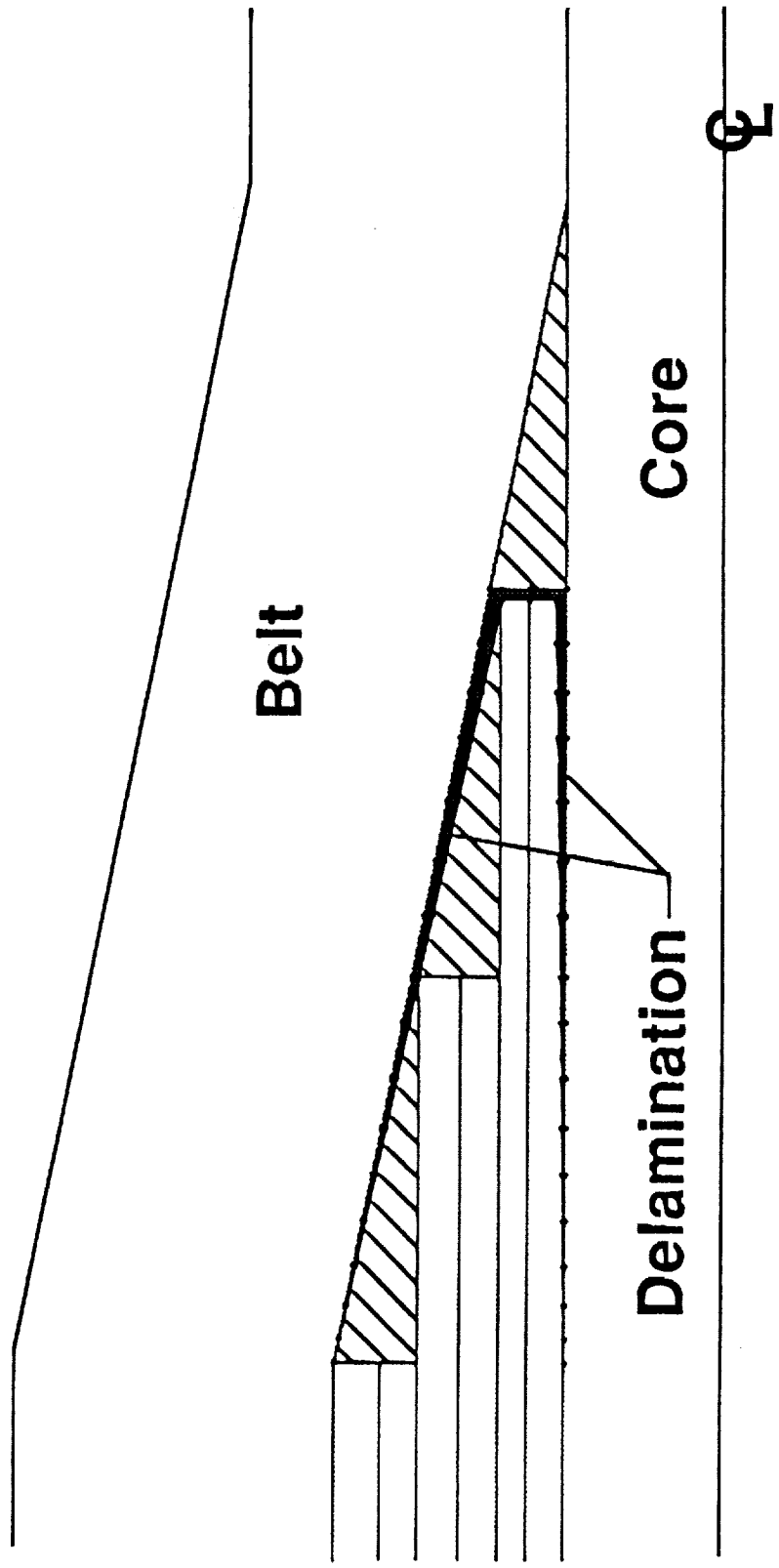
Figure 9. - Schematic of initial delamination damage.
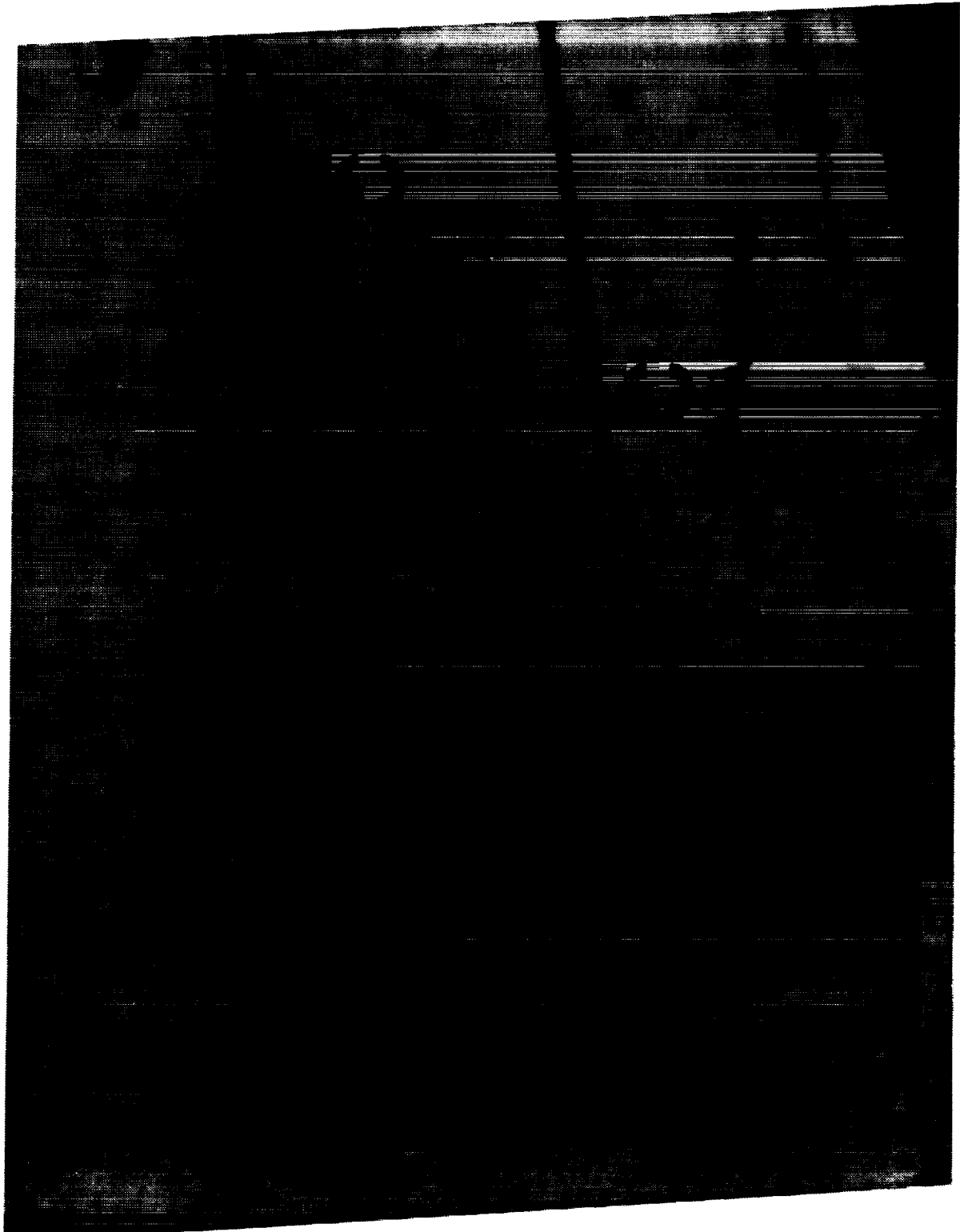
Figure 10. - Final delamination failure in IM6/1827I.
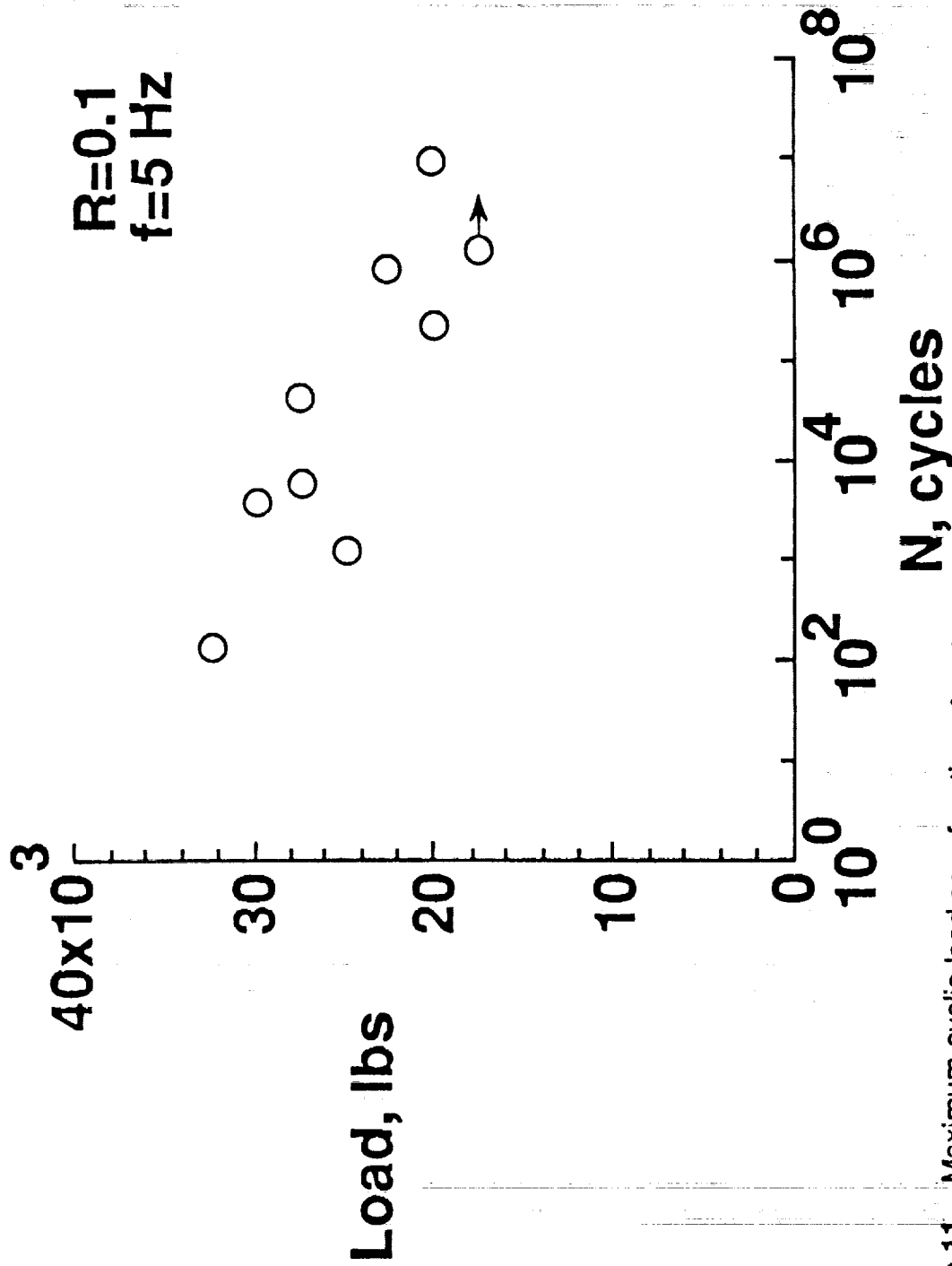
Figure 11. - Maximum cyclic load as a function of cycles to unstable delamination onset in IM6/1827I, Type T.
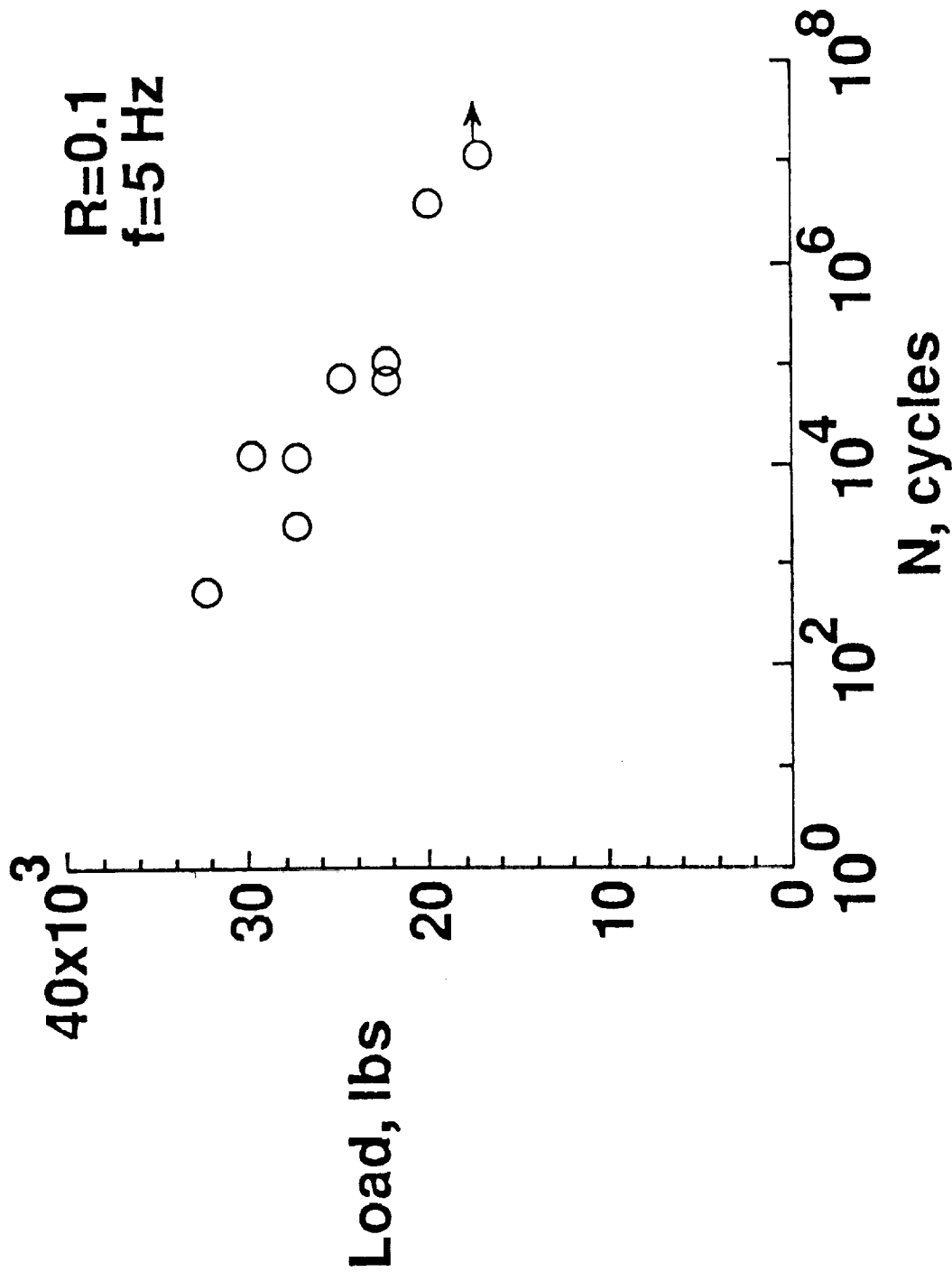
Figure 12. - Maximum cyclic load as a function of cycles to unstable
delamination onset in IM6/1827I, Type C.
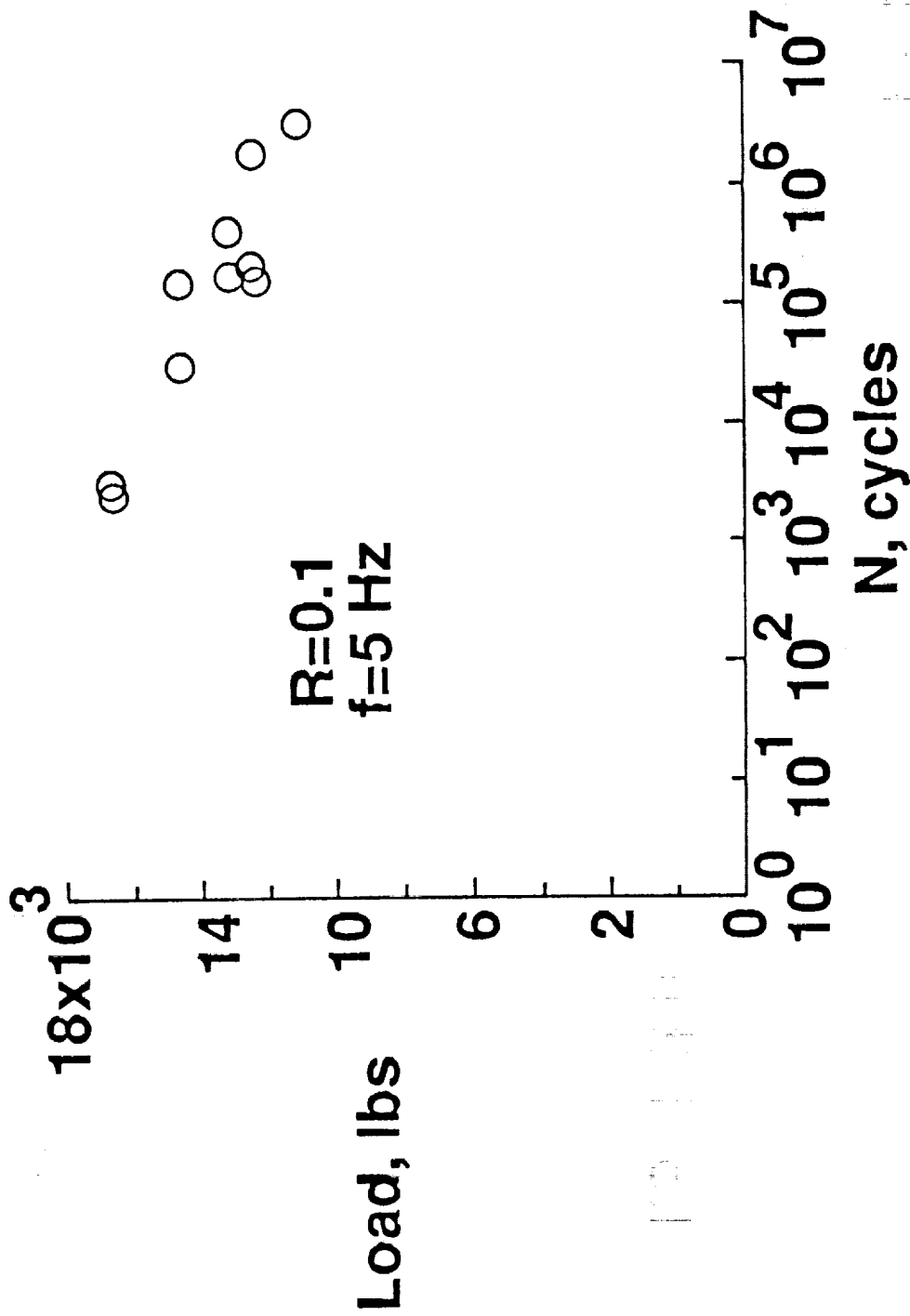
Figure 13. - Maximum cyclic load as a function of cycles to unstable delamination onset in S2/CE9000.
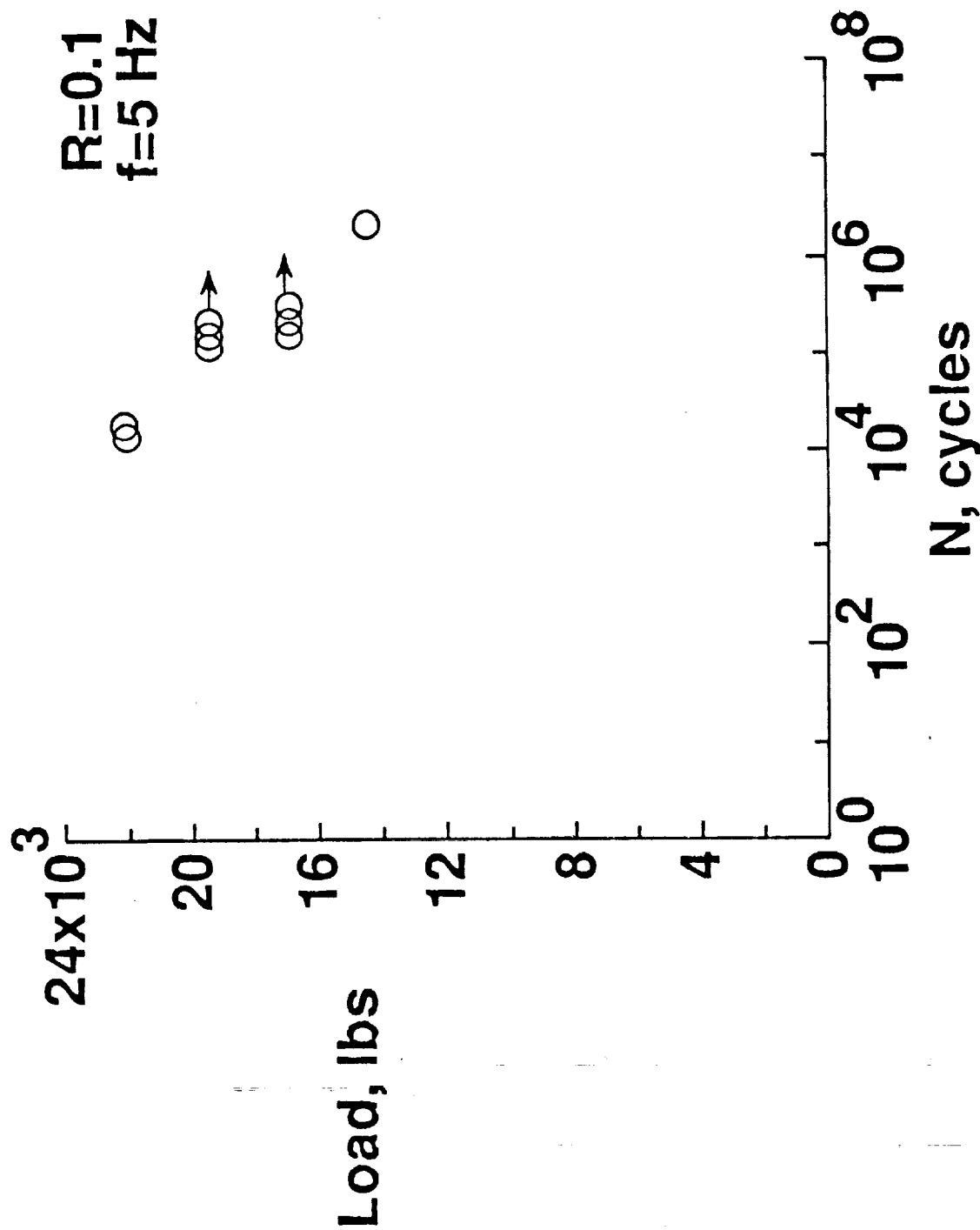
Figure 14. - Maximum cyclic load as a function of cycles to unstable delamination onset in S2/SP250.
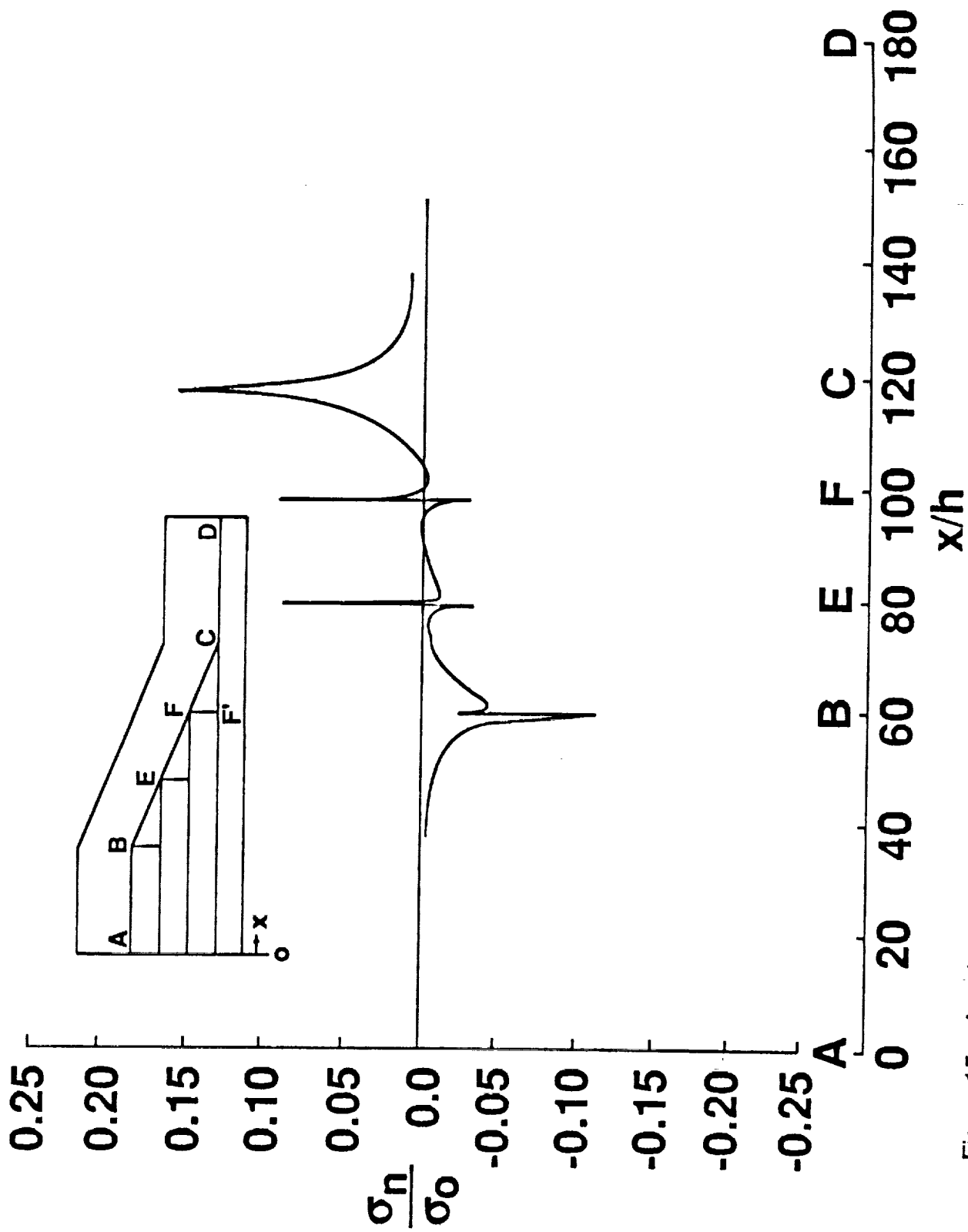
Figure 15. - Interlaminar normal stresses in IM6/1827I laminate with no initial delamination.

44

Figure 16. - Interlaminar shear stresses in IM6/1827I laminate with no initial delamination.

45

Figure 17. - Interlaminar normal stresses in IM6/1827I laminate with resin crack.

Figure 18. – Interlaminar shear stresses in IM6/18271 laminate with resin crack.
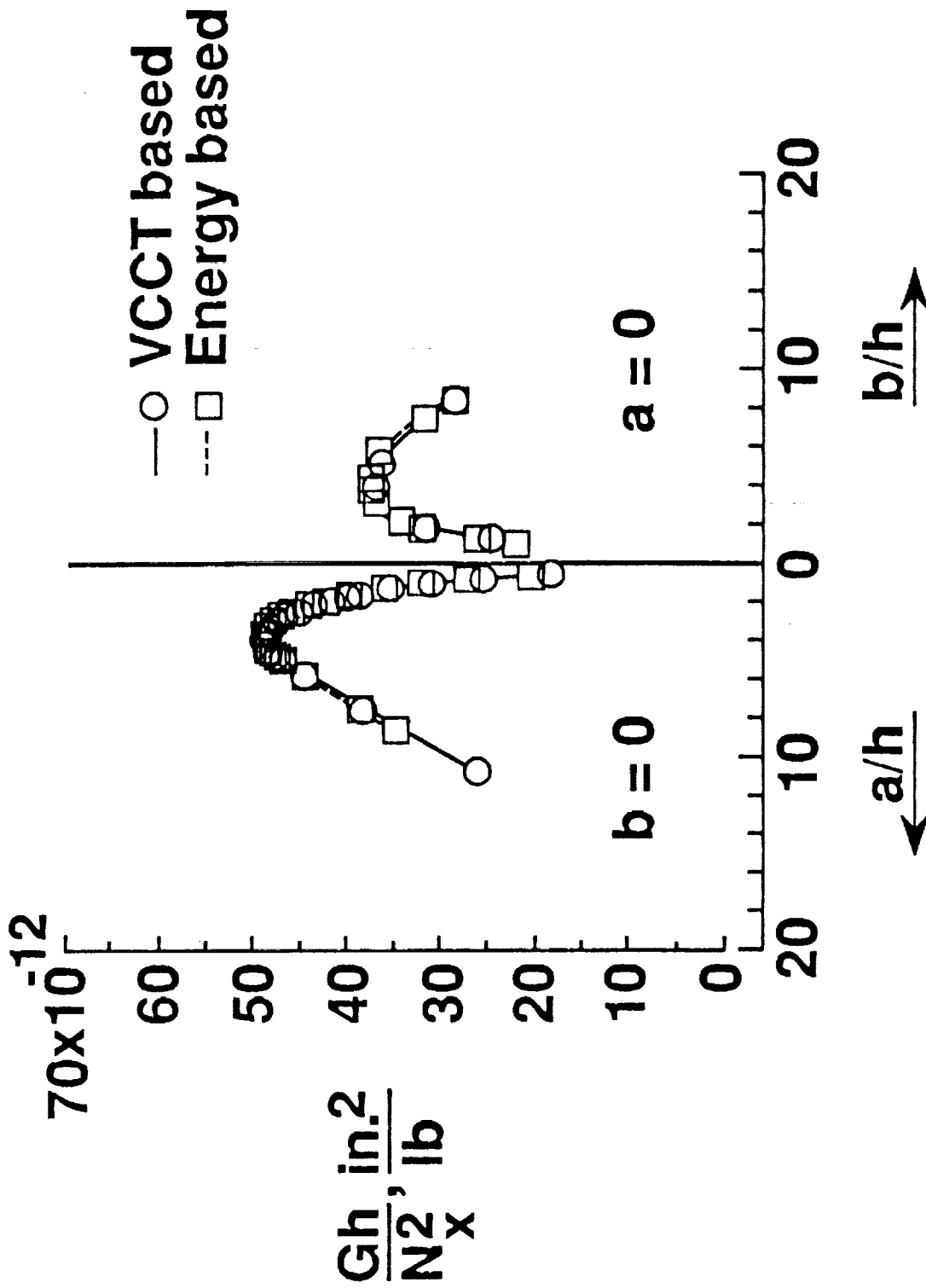
Figure 19. - Normalized strain energy release rate for IM6/1827I laminate with no initial delamination.
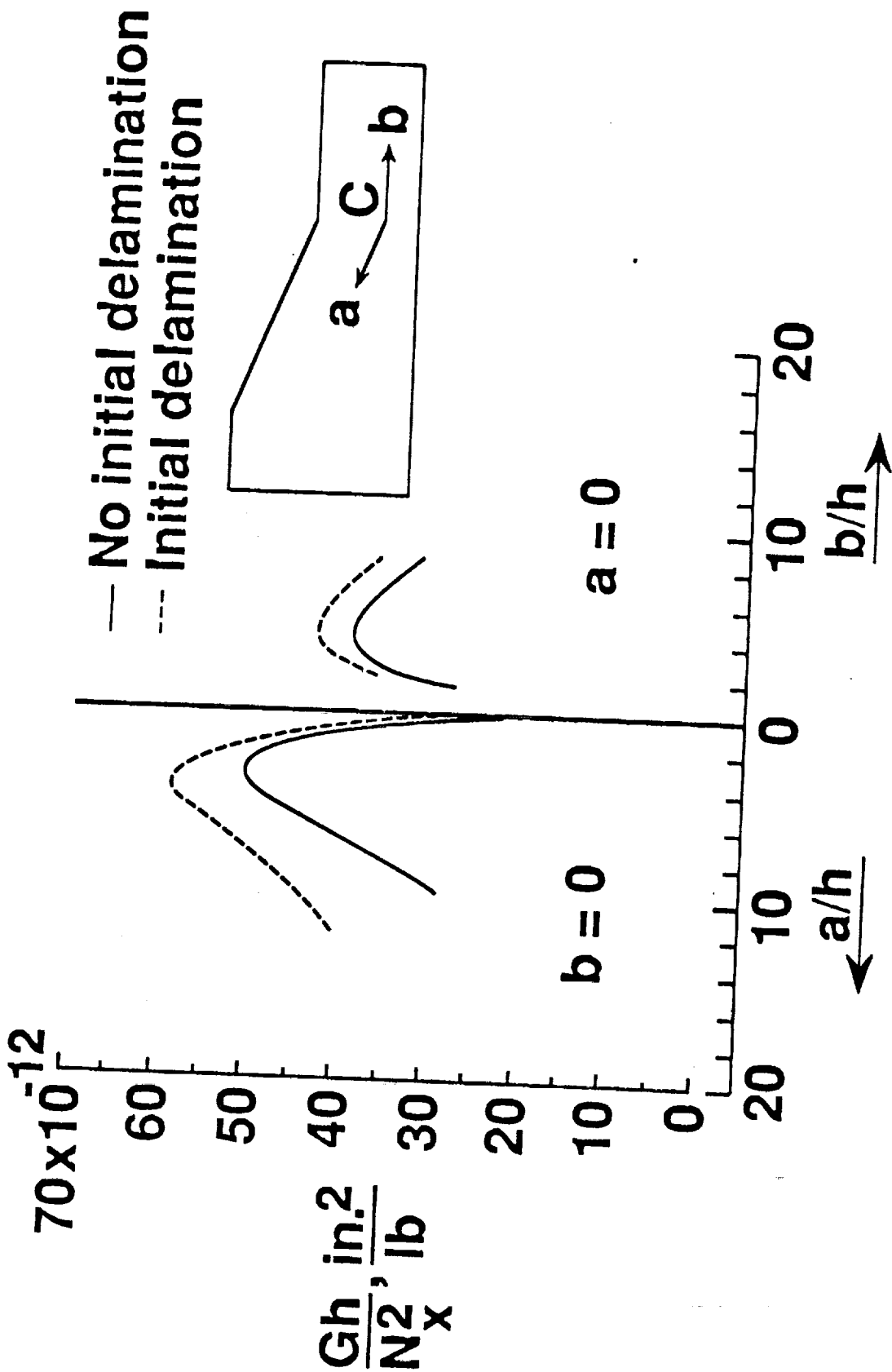
Figure 20. - Normalized strain energy release rates for IM6/18271 laminate.
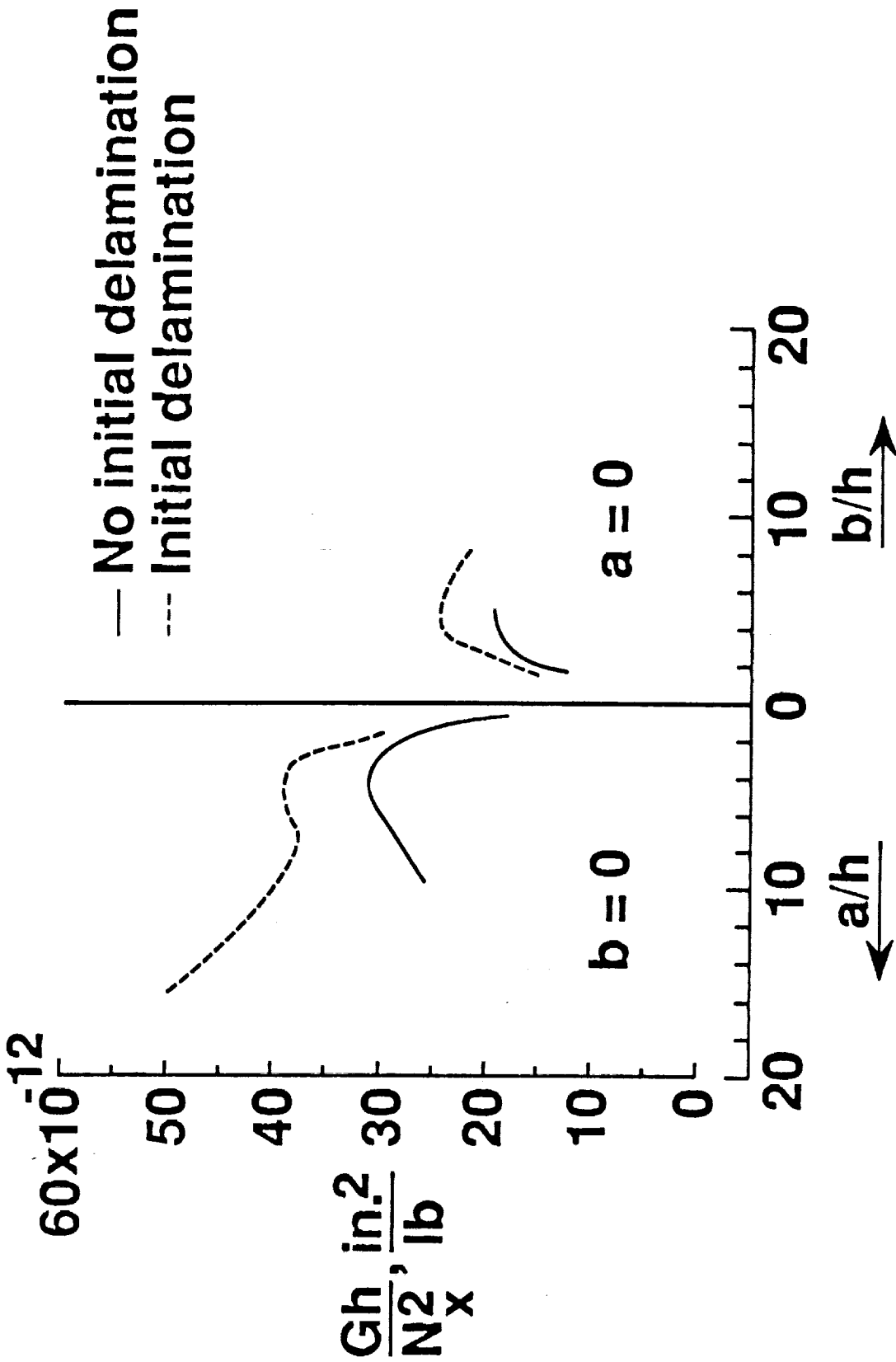
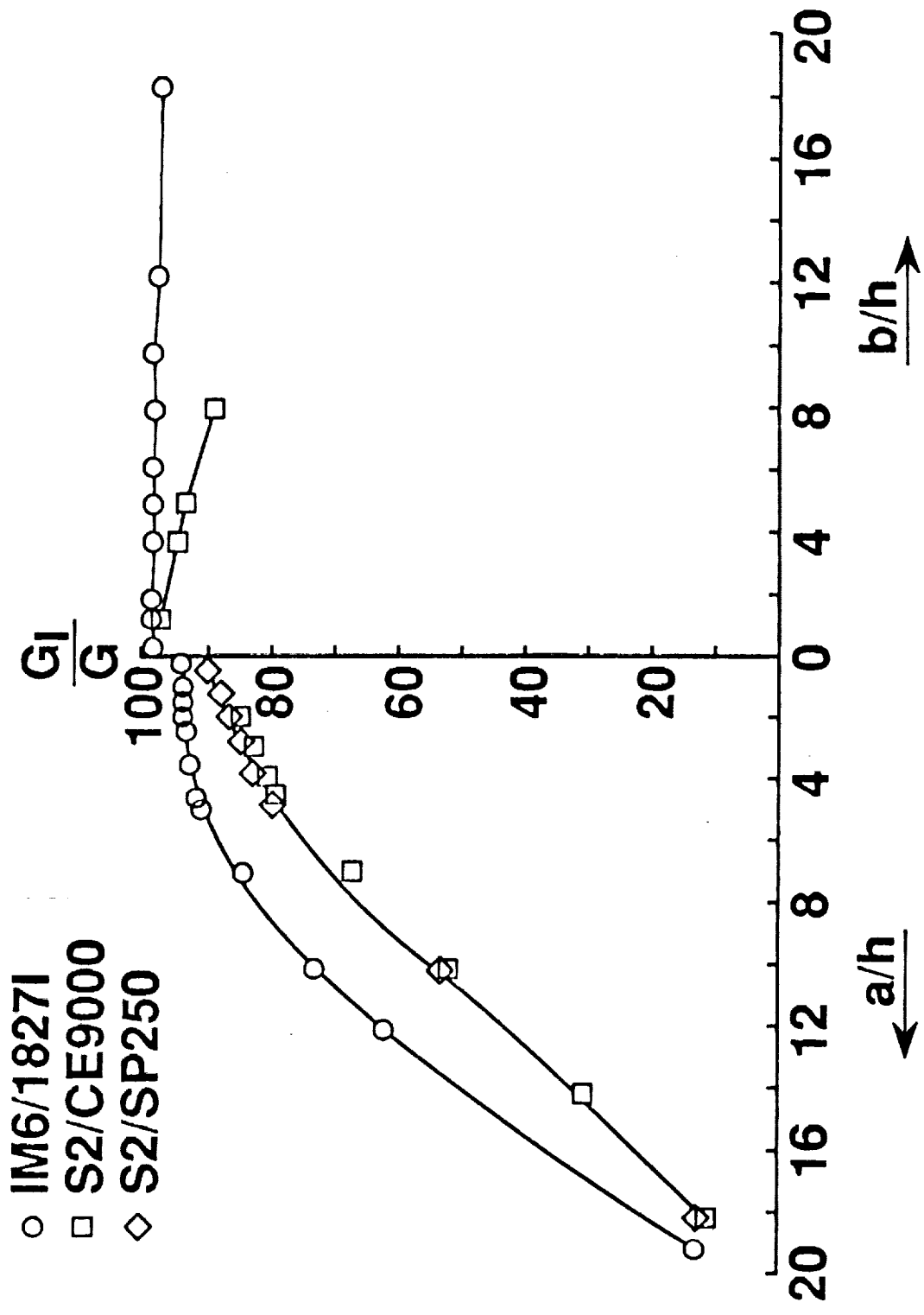Figure 21. - Normalized strain energy release rates for S2/CE9000 laminate.
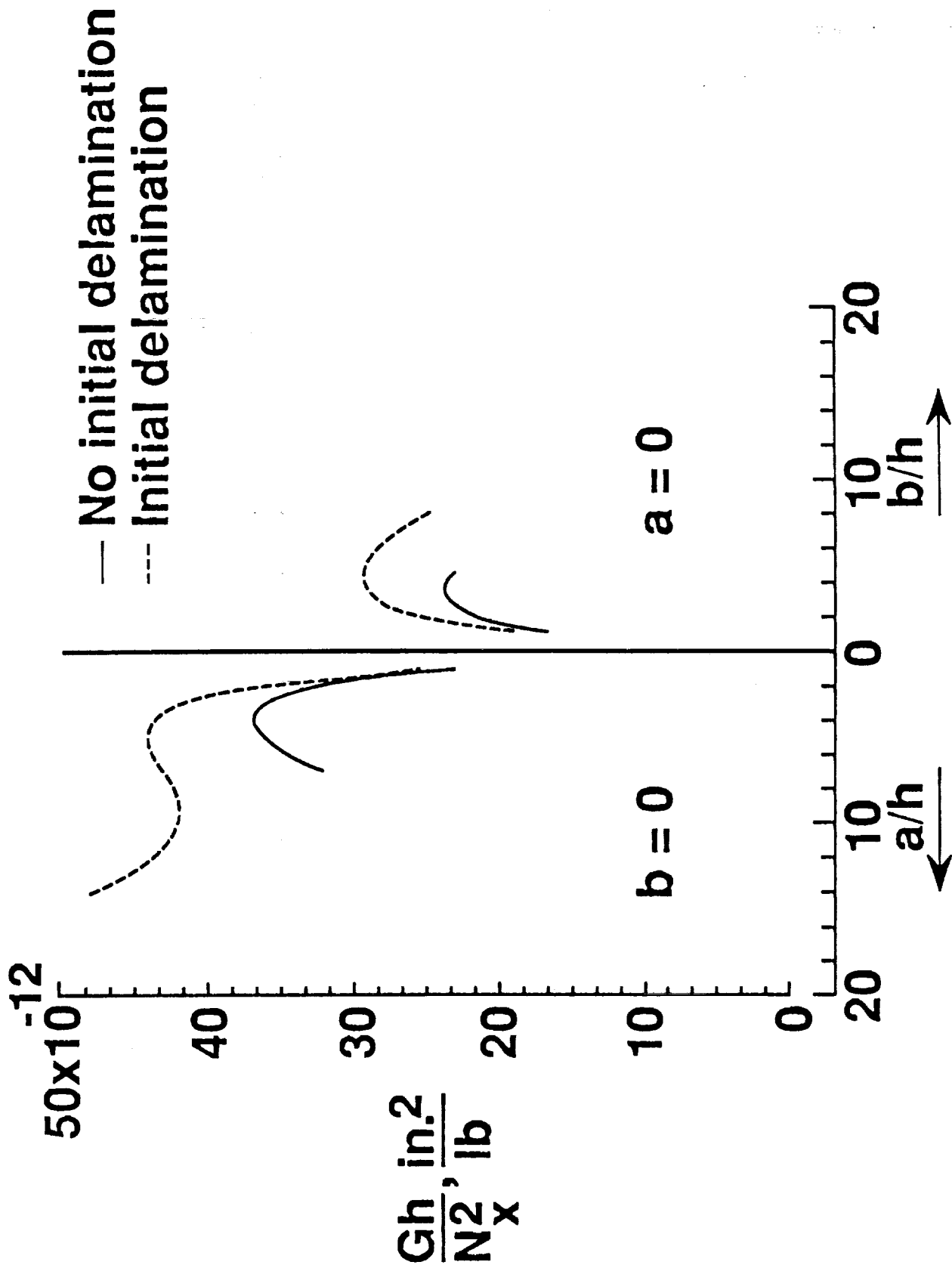
Figure 22. - Normalized strain energy release rates for S2/SP250 laminate.

51

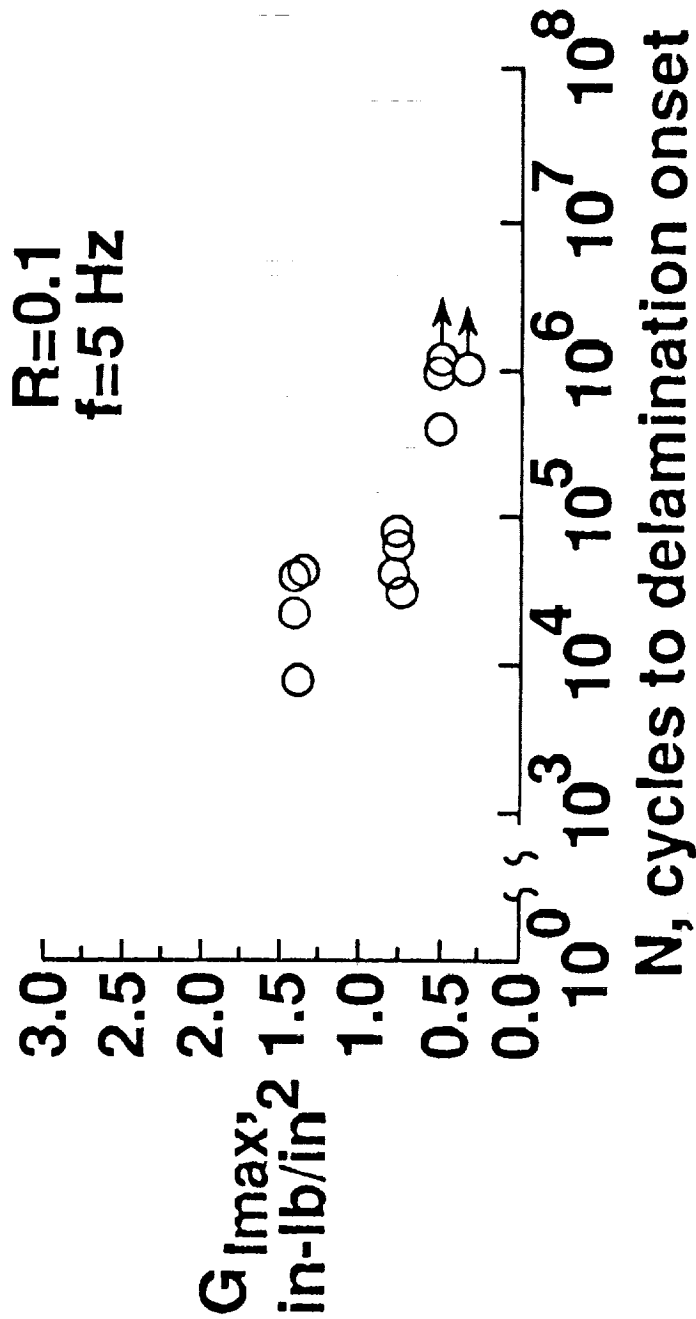Figure 23. - Ratio of $G_I$ to total $G$ for delamination growth in laminate with initial delamination.

Figure 24. - $G_{Imax}$ as a function of cycles to delamination onset for IM6/1827I.
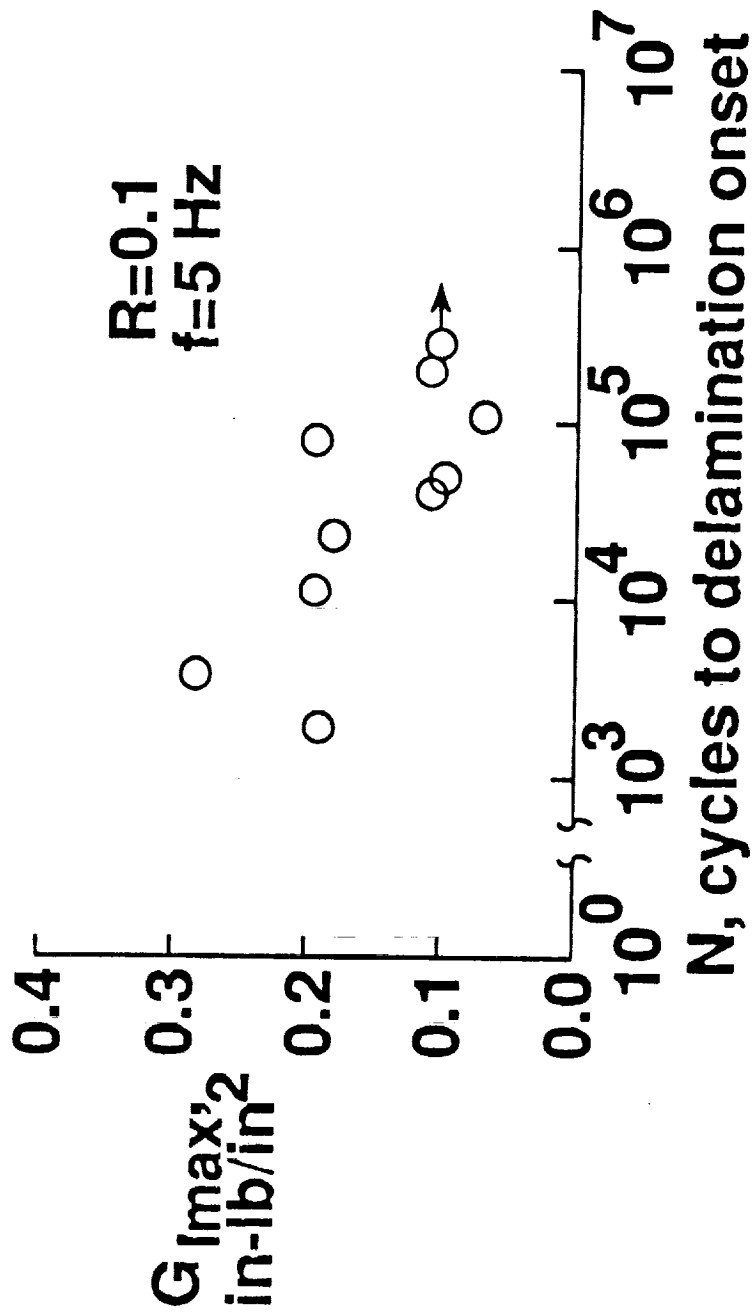
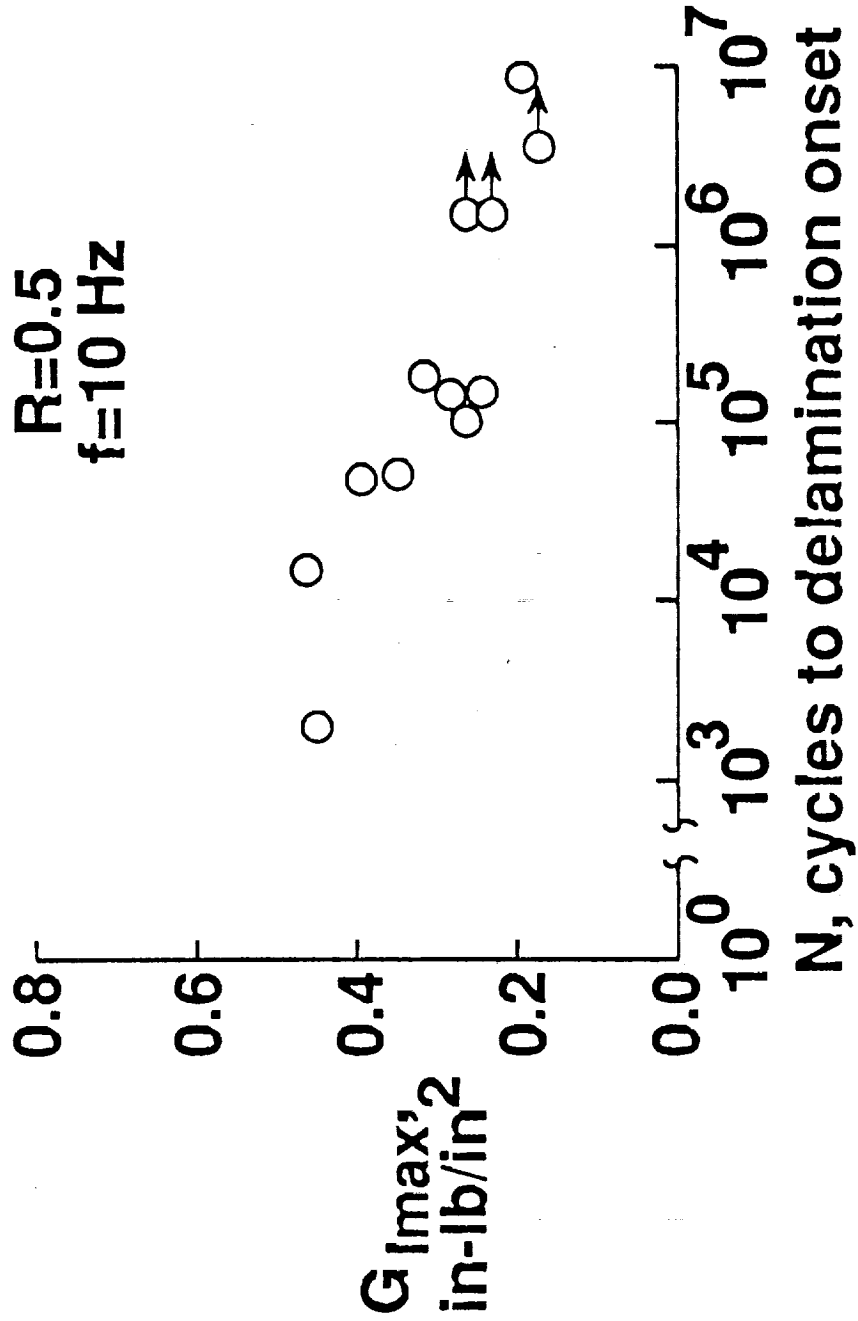Figure 25. - $G_{Imax}$ as a function of cycles to delamination onset for S2/CE9000.

Figure 26. - $G_{Imax}$ as a function of cycles to delamination onset for S2/SP250.
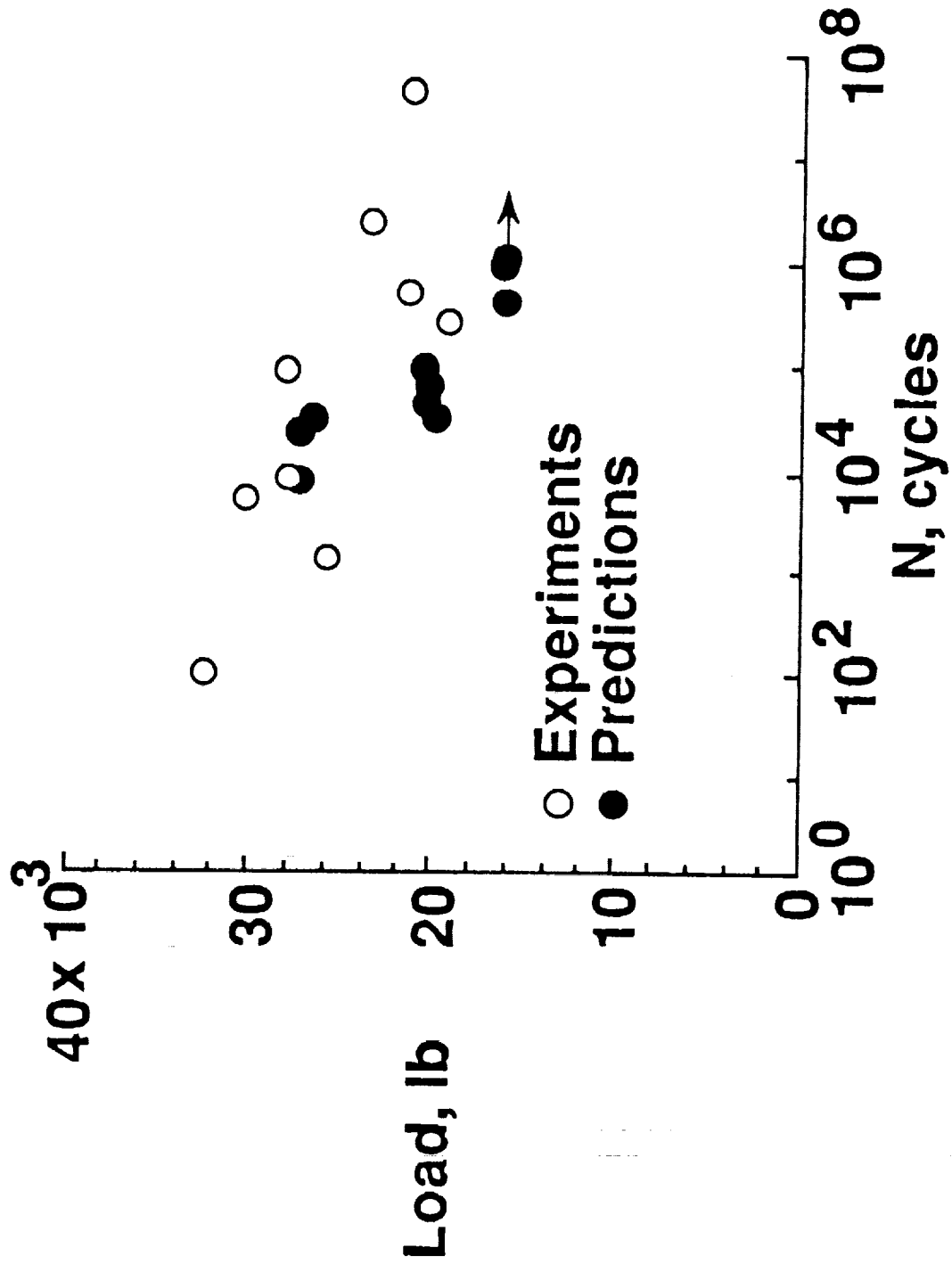
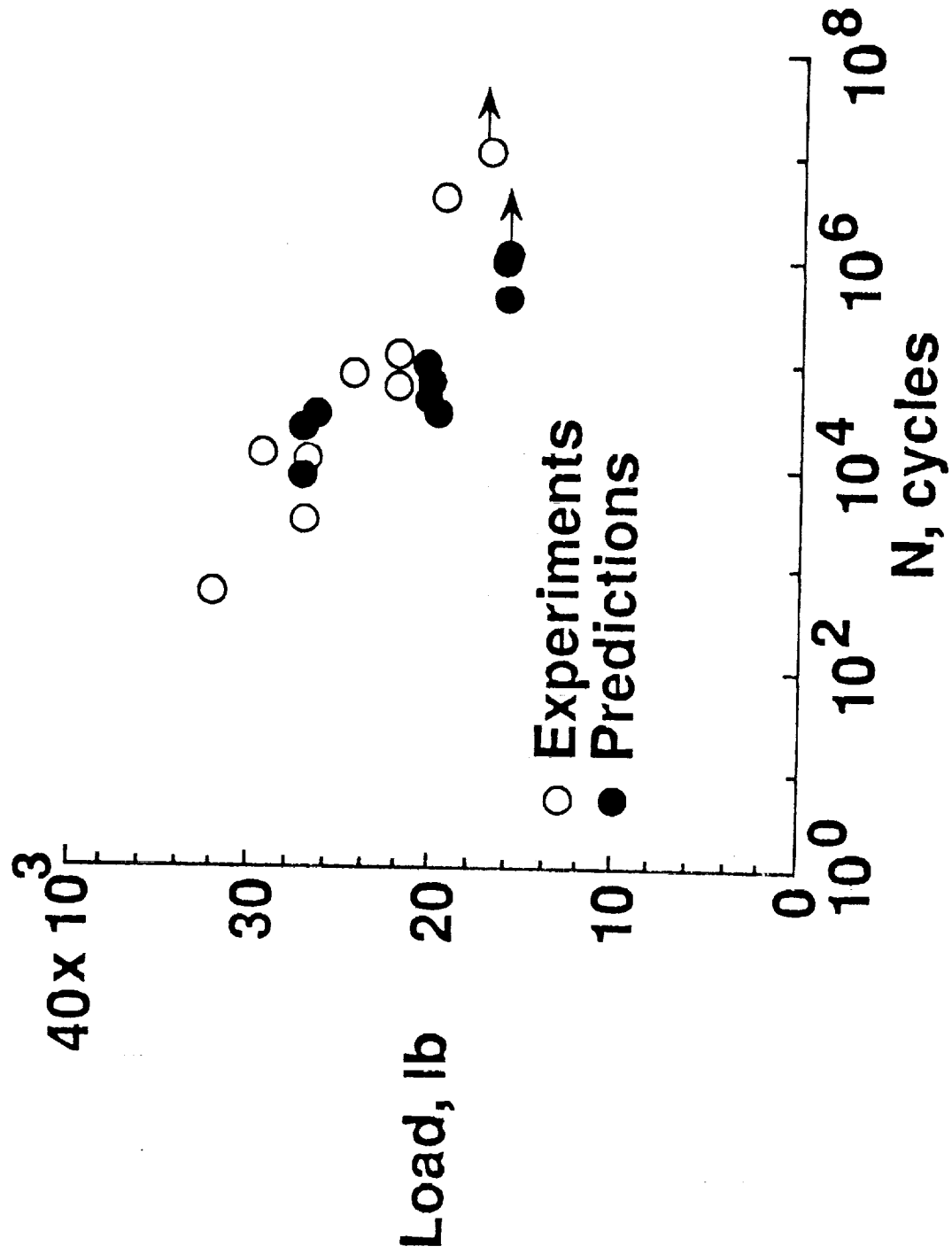Figure 27. - Predicted and measured delamination onset in fatigue for IM6/1827I laminates, Type T.

Figure 28. - Predicted and measured delamination onset in fatigue for IM6/18271 laminates, Type C.
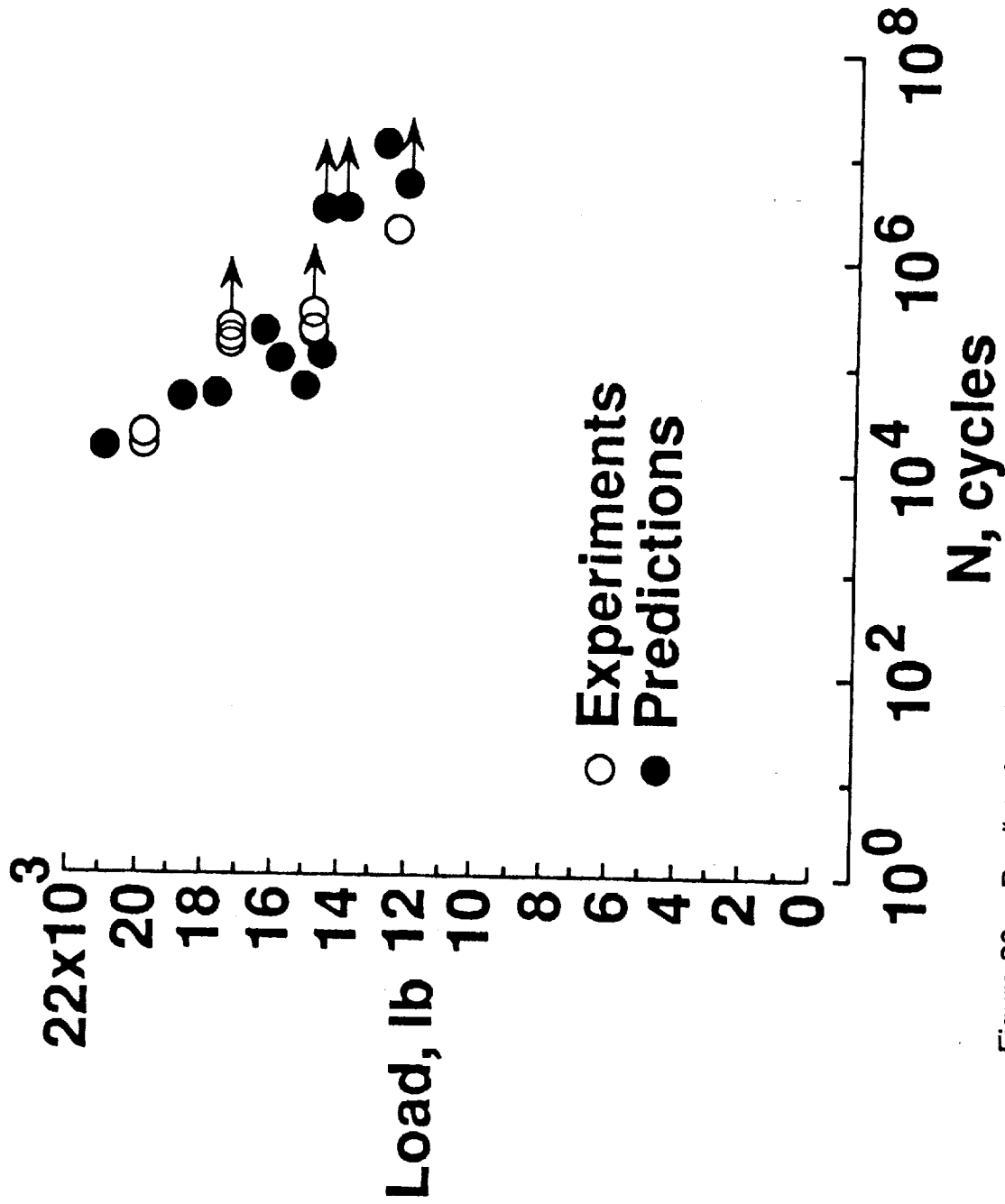
Figure 29. - Predicted and measured delamination onset in fatigue for S2/CE9000 laminates.
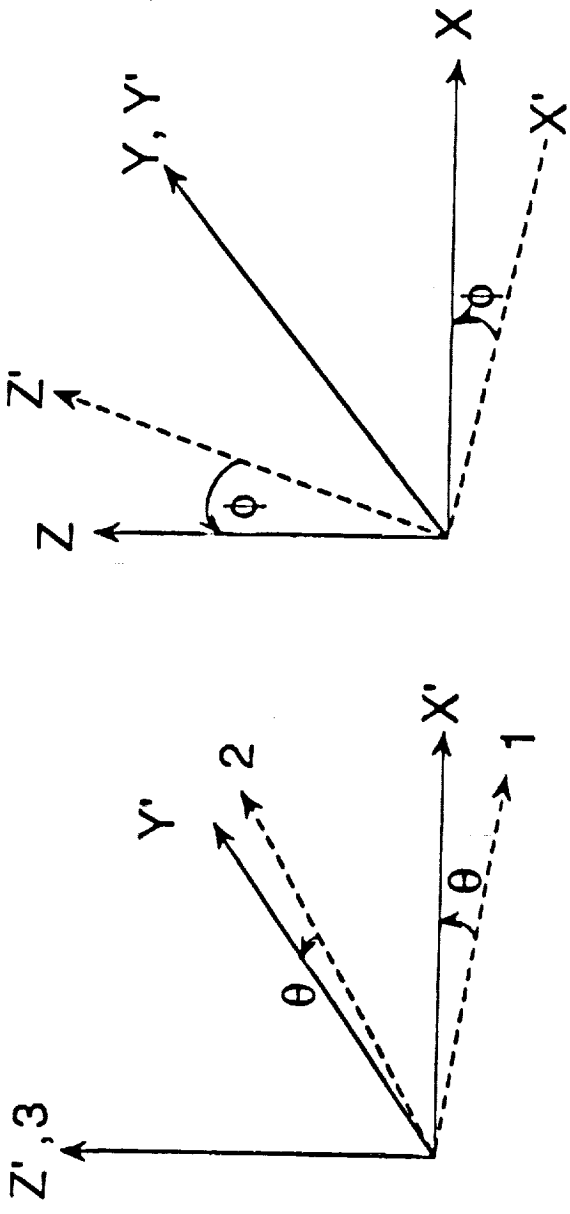
Figure 30. - Predicted and measured delamination onset in fatigue for S2/SP250 laminates.

1, 2, 3: Material system
rotation $\theta$ about 3 axis

X, Y, Z: Global coordinate system
rotation $\phi$ about Y' axis

Figure 31. - Transformation from material coordinate system
to global coordinate system.

60

# NASA

National Aeronautics and Space Administration

# Report Documentation Page

| 1. Report No. NASA TM-101673 AVSCOM TM-89-B-011 | 2. Government Accession No. | 3. Recipient's Catalog No. |
|---|---|---|

| 4. Title and Subtitle | | 5. Report Date |
|---|---|---|
| Fatigue Delamination Onset Prediction in Tapered Composite Laminates | | December 1989 |
| | | 6. Performing Organization Code |

| 7. Author(s) | 8. Performing Organization Report No. |
|---|---|
| Gretchen B. Murri*; Satish A. Salpekar**; and T. Kevin O'Brien* | |
| | 10. Work Unit No. 505-63-01-05 |

| 9. Performing Organization Name and Address | 11. Contract or Grant No. |
|---|---|
| NASA Langley Research Center, Hampton, VA 23665-5225 U.S. ArmyAviation Research and Technology Activity (AVSCOM) Aerostructures Directorate Hampton, VA 23665-5225 | |
| | 13. Type of Report and Period Covered |

| 12. Sponsoring Agency Name and Address | |
|---|---|
| National Aeronautics and Space Administration Washington, DC 20546-0001 U.S. Army Aviation Systems Command St. Louis, MO 63166 | Technical Memorandum |
| | 14. Sponsoring Agency Code |

15. Supplementary Notes

*U.S. Army Aerostructures Directorate, USAARTA-AVSCOM
**Analytical Services and Materials, Inc., Hampton, VA

16. Abstract

Tapered [0°] laminates of S2/CE9000 and S2/SP250 glass/epoxies, and IM6/1827I graphite/epoxy were tested in cyclic tension. The specimens usually showed some initial stable delaminations in the tapered region, but these did not affect the stiffness of the specimens, and loading was continued until the specimens either delaminated unstably, or reached $10^6$ to $2 \times 10^7$ million cycles with no unstable delamination. The final unstable delamination originated at the junction of the thin and tapered regions.

A finite-element model was developed for the tapered laminate with and without the initial stable delaminations observed in the tests. The analysis showed that for both cases the most likely place for an opening (Mode I) delamination to originate is at the junction of the taper and thin regions. For each material type, the models were used to calculate the strain energy release rate, G, associated with delaminations originating at that junction and growing either into the thin region or tapered region.

For the materials tested, cyclic $G_{Imax}$ values from DCB tests were used with the maximum strain energy release rates calculated from the finite-element analysis to predict the onset of unstable delamination at the junction as a function of fatigue cycles. The predictions were compared to experimental values of maximum cyclic load as a function of cycles to unstable delamination from fatigue tests in tapered laminates. For the IM6/1827I and the S2/SP250 laminates, the predictions agreed very well with the test data. Predicted values for the S2/CE9000 were conservative compared to the test data.

| 17. Key Words (Suggested by Author(s)) | 18. Distribution Statement |
|---|---|
| Strain energy release rate DCB Finite element Interleaf Dropped ply | Unclassified - Unlimited Subject Category - 39 |

| 19. Security Classif. (of this report) | 20. Security Classif. (of this page) | 21. No. of pages | 22. Price |
|---|---|---|---|
| Unclassified | Unclassified | 61 | A04 |

NASA FORM 1626 OCT 86